Measurement of the Most Important Physics Quantity Ever Discovered

by

Kiyotaka Akabori

Advised by Professor John F. Nagle and Stephanie Tristram-Nagle

June 3, 2014

Abstract

Protein function essential for living organisms is regulated by cell membranes. The building blocks of cell membranes are the lipid bilayers, into which lipid molecules in water self-assemble. Lipid bilayers show rich phase behavior. Among the thermodynamic phases observed in lipid bilayer systems is the ripple phase where the ripple is asymmetric and sawtooth-like, consisting of a longer and shorter arm, connected by a kink. Study of the ripple phase properties contributes to our understanding of the balance of forces within the lipid bilayers and the resulting molecular organization. Various theories have been developed in order to explain the appearance of this kink, with each theory predicting different molecular organization within the lipid bilayers. However, the molecular organization in the ripple phase has not been determined yet. In this paper, we report the results of the high-resolution wide angle X-ray scattering from the ripple phase. The observed sharp peaks indicates that lipid molecules are tightly packed, exhibiting short-range order. Furthermore, the observed X-ray scattering pattern is consistent with slight disordering of lipids in the kink regions.

Acknowledgments

I would like to express my profound gratitude to my advisor and I thank everybody else, too. I would like to express my profound gratitude to my advisor and I thank everybody else, too. I would like to express my profound gratitude to my advisor and I thank everybody else, too. I would like to express my profound gratitude to my advisor and I thank everybody else, too. I would like to express my profound gratitude to my advisor and I thank everybody else, too.

Contents

List of Tables

List of Figures

Chapter 1

Introduction

Biomembranes are blah blah blah. Various thermodynamic phases exist (see fig). In this thesis, we forcus on the fluid and ripple phase. In the former phase, we investigated the interaction of a peptide called Tat with lipid bilayers in the fluid phase. The overview on this field is discussed in section 1.1. The results and interpretation are discussed in chapter 3 and 4. Regarding the ripple phase, we measured the electron density profile of the lipid bilayers using a stack of oriented bilayers. Using wide angle x-ray scattering technique, we also investigated the chain packing within a bilayer. The overview is discussed in section 1.2. The results and interpretation are discussed in chapter 5 and 6. The appendices show a lot of details that will allow other people to reproduce much of the results shown in this thesis as well as help readers understand scattering analysis employed in this work. It is the author's hope that these details will help future researchers, especially students, understand some of the techniques to investigate the structure of lipid bilayers in sub Angstrom resolution.

1.1   HIV life cycle

Basically, this section will introduce what HIV does to human cells in order to put Tat in a context. Follow some of the review papers on HIV.

1.2   Overview of Tat

The name cell-penetrating peptide (CPP) connotes a peptide that easily penetrates cell membranes (for Reviews see [1-3]).

This thesis focuses on the transactivator of translation, Tat, from the HIV-1 virus, which plays a role in AIDS progression. Earlier work showed that the HIV-Tat protein (86 amino acids) was efficiently taken up by cells, and concentrations as low as 1 nM were sufficient to transactivate a reporter gene expressed from the HIV-1 promoter [4, 5]. It has been reported that Tat protein uptake does not require ATP

[6]. Studies using inhibitors of different types of endocytosis, including clathrinand caveolae-mediated, or receptor-independent macropinocytosis reached the same conclusion that ATP mediated endocytosis is not involved in Tat protein permeation [7-10]. However, this issue is controversial, as other studies found evidence for endocytosis in Tat protein import [11-19]. Still other studies have concluded that an ATP requirement for Tat protein entry depends on the size of the cargo attached to Tat protein, or on the specific cell type [20-22]. The part of the Tat protein responsible for cellular uptake was assigned to a short region Tat (48-60), G48RKKRRQRRRPPQ60, which is particularly rich in basic amino acids [6]. Deletion of three out of eight positive charges in this region caused loss of its ability to translocate [6]. In this manuscript short basic regions will be called Tat, while the entire 86- amino acid protein will be called Tat protein. Tat was shown to be responsible for the Tat proteins permeation into the cell nucleus and the nucleoli [6], and this was confirmed using live cell fluorescence in SVGA cells [23]. Tat (48-60) was shown to have little toxicity on HeLa cells at 100 M concentration [6], but the longer Tat protein (2-86) was toxic to rat brain glioma cells at 1-10 M [24]. Interestingly, no hemolytic activity was found when human erythrocytes were incubated with a highly neurotoxic concentration (40 M) of Tat (2-86) [24]. These results prompt the question, what is the mechanism of Tats translocation through membranes? To address this question, many biophysical studies have used simple models of biological membranes composed of a small number of lipid types. These studies are valuable because there is no possibility for ATP-dependent translocation, thus ruling out endocytosis if translocation occurs. For example, Mishra et al. reported that the rate of entry into giant unilamellar vesicles (GUVs) composed of PS/PC (1:4 mole ratio) lipids of rhodamine-tagged Tat is immeasurably slow, but it crosses a GUV composed of PS/PC/PE (1:2:1) lipids within 30 seconds [25]. This study suggests that negative curvature induced by the inclusion of PE facilitates translocation. In a subsequent study using much smaller unilamellar vesicles (LUVs), Tat did not release an encapsulated fluorescent probe in LUVs composed of lipids modeling the outer plasma membrane, PC/PE/SM/Chol (1:1:1:1.5), but did release the probe in LUVs composed of BMP/PC/PE (77:19:4) [26]; BMP (bis(monoacylglycero)-phosphate) is an anionic lipid specific to late endosomes. In that study [26], the inclusion of PE did not suffice to cause leaky fusion in LUVs in the absence of a negatively charged lipid. The contrasting results in these two experiments may also be due to the use of LUVs instead of GUVs since it was reported that Tat does not translocate across LUVS of PC/PG (3:2) but does translocate across GUVs of the same lipid composition [27]. In a similar experiment, Tat did not translocate into egg PC LUVs [28]. In another experiment confirming these results, Tat did not translocate into GUVS containing only PC with 20 molwith PC, then rapid translocation of Tat was observed [29]. These experiments demonstrate that the choice of lipids and model systems influences Tat translocation.

Is a pore formed during Tat translocation? Although direct conductance measurements of Tat and lipid membranes have not been carried out, two studies mea-

sured conductance with the somewhat similar CPP oligoarginine R9C peptide. Using single-channel conductance of gramicidin A in planar lipid membranes consisting of anionic, neutral or positively charged lipids, R9C did not increase conductance, even in anionic lipid membranes [30]. By contrast, in a similar experiment using planar lipid membranes, a current was induced by R9C in PC/PG (3:1) membranes, with increasing destabilization over time [31]. Thus questions remain about pore formation of Tat in membranes. In the GUV experiment with Tat mentioned above [29], Ciobanasu et al., using size exclusion methods, suggested a pore in the nanometer range, which could only be passed by small dye tracer molecules. Thus, if a true pore forms, it is likely to be small and transitory.

What is the secondary structure of Tat in membranes? Circular dichroism (CD) spectroscopy was carried out on, where the penultimate proline on Tat (48-60) was replaced by a tryptophan [27]. That study found a random coil secondary structure in aqueous solution as well as when mixed with PC/PG/PE (65:35:5) LUVs. The same result was obtained using CD in PC/PG (3:1) vesicles by Ziegler et al.[10], indicating that an alpha helix is not required for Tats translocation ability. In addition, solid state NMR has identified a random coil structure of Tat in DMPC/DMPG (8:7 mole ratio) multibilayers [32]. In the larger Tat-(1-72)-protein NMR measurements at pH 4 have determined there is no secondary structure, with a dynamical basic region [33]. Similarly, NMR was used to study the full Tat protein and found a highly flexible basic region [34].

Regarding the mechanism of translocation of this randomly structured, short basic peptide, many models have been proposed based on the conflicting results listed above. Molecular dynamics simulations offer some insight into the molecular details of translocation. Herce and Garcia simulated the translocation of Tat (Y47GRKKRRQRRR57) across DOPC at various lipid:peptide molar ratios [35]. Their simulations indicated that Tat binds to the phosphate headgroups, with 1 Tat binding with 14 lipids, each positive charge on Tat associated with nearly 2 phosphate groups [35]. Translocation involved a localized thinning, and snorkeling of arginine side chains through the hydrophobic layer to interact with phosphates on the other side of the membrane. This allowed some water molecules to penetrate the membrane along with Tat, forming a pore [35]. In this simulation, performed without inclusion of counterions, pore formation was only observed at high ratios of peptide:lipid (1:18) or at elevated temperature. However, a subsequent Gromacs simulation with counterions found no thinning and no pore formation when Tat was added to DOPC membranes [36]. Instead it found a membrane invagination associated with a cluster of Tat peptides, suggesting that micropinocytosis could be the model for Tat translocation across membranes [36]. In this work we primarily combine experimental low-angle X-ray scattering (LAXS) data with MD simulations to obtain the structure of fully hydrated, oriented lipid bilayers with Tat (47-57) added at several mole ratios. The lipid systems were DOPC, DOPC/DOPE (3:1 mole ratio), DOPC/DOPS (3:1), DOPC/DOPE (1:1) and a mimic of the nuclear membrane

(POPC/POPE/POPS/SoyPI/Chol, 69:15:2:4:11). Accessory techniques, densitometry, wideangle X-ray scattering (WAXS), neutron scattering, CD spectroscopy were also applied to further characterize Tat/membrane interactions.

Chapter 2

Experiment and Simulation

2.1 X-ray optics

High resolution setup should be described.
Low resolution setup should be described.
Detector correction was applied. See references.

2.2 Hydration Chamber

The chamber is sealed very tightly. We used helium to replace air. Air scattering is strong. Mylar window, cast scatteing in wide angle region. Helium. Peltier used to condense water in and out of the sample.

2.3 Sample Preparation

Synthesized lipids were purchased from Avanti Polar Lipids (Alabaster, AL) and used without further purification. Membrane mimics were prepared by first dissolving lyophilized lipids in chloroform and then mixing these stock solutions to create the lipid compositions DOPC, DOPC/DOPE (3:1), DOPC/DOPE (1:1), DOPC/DOPS (3:1) and nuclear membrane mimic (POPC/POPE/POPS/SoyPI/Cholesterol, 69:15:2:4:11) (based on Ref. [37]). Peptide (Y47GRKKRRQRRR57) was purchased in two separate lots from the Peptide Synthesis Facility (University of Pittsburgh, Pittsburgh, PA); mass spectroscopy revealed greater than 95% purity. This Tat peptide corresponds to residues (47-57) of the 86 residues in the Tat protein [6]. Tat was dissolved in HPLC trifluoroethanol (TFE) and then mixed with lipid stock solutions in chloroform to form mole fractions between 0.0044 and 0.108. Weight of Tat in these mole fractions was corrected for protein content (the remainder being 8 trifluoroacetate counter-ions from the peptide synthesis). Solvents were removed by evaporation in the fume hood followed by 2 hours in a vacuum chamber at room temperature.

2.4 Samples for X-ray scattering

Four mg dried lipid/peptide mixture was re-dissolved in HPLC chloroform/TFE (2:1 v:v) for most of the lipid compositions. DOPC/DOPS (3:1) mixtures required chloroform/HFP (1:1 v:v) in order to solubilize the negatively charged DOPS. 200 l of 4 mg mixtures in solvents were plated onto silicon wafers (15x30x1 mm) via the rock and roll method [38] to produce stacks of 1800 well-aligned bilayers; solvents were removed by evaporation in the fume hood, followed by two hours under vacuum. Samples were prehydrated through the vapor in polypropylene hydration chambers at 37 °Cfor two to six hours directly before hydrating in the thick-walled X-ray hydration chamber [39] for 0.51 h. Pre-equilibration allowed sufficient time for equilibrium binding of peptides with membrane mimics.

For ripple phase experiments, the sample was annealed at 60 °Cfor approximately 10 hours prior to the experiment. The sample was trimmed to 1 mm for high resolution and 5 mm for low resolution study, respectively. The temperature was set at 18 °C. The sample was dried by applying a small heating current to the Peltier.

2.5 Low Angle X-ray Scattering Experiment

The analysis of diffuse low angle X-ray scattering from oriented stacks of fluctuating fluid bilayers has been previously described [39]. Absolute form factors —F(qz)— were obtained as previously described [42]. Modeling to estimate the locations of Tat and the lipid components was performed using the SDP program [44].

2.6 Transmission X-ray Scattering Experiment

Transmission experiment. The axis of rotation does not coincide with the plane of the sample, so that the sample-to-detector distance is not fixed for different motor angle. The sample-to-detector distance was estimated from the setup geometry. We used 35 μm thin Si wafer, which absorbs x-ray by only 10%.

2.7 Densimetry

2.7.1 Samples for densimetry

Multilamellar vesicles (MLVs) were prepared by mixing dried lipid mixtures with MilliQ water to a final concentration of 2-5 wt% in nalgene vials and cycling three times between -20oC and 60oC for ten minutes at each temperature with vortexing. Pure Tat was dissolved in water at 0.4 wt%.

2.7.2 Densimetry

Volumes of lipid mixtures with and without peptides in fully hydrated multilamellar vesicles (MLV) were determined at 370.01 °Cusing an Anton-Paar USA DMA5000M (Ashland, VA) vibrating tube densimeter [47].

2.8 MD simulation

Systems with different DOPC/Tat mole ratios (128:0, 128:2 and 128:4, corresponding to 0, 0.015 and 0.030 mole fractions) were simulated atomistically using the Gromacs 4.6.1 package [49]. DOPC was modeled by the Slipid force field [50, 51] and HIV Tat was modeled by Amber 99SB [52]. Tip3p water was used [53]. The number of Tats was divided equally on each side of the bilayer to mimic experimental conditions. All systems were simulated at 310 K with a constant area in the x-y plane for and 1 atm constant pressure in the Z direction. Each system was simulated for 100 ns and the last 50 ns was used as the production run. At each DOPC/Tat mole ratio, we studied systems with three different area/lipid (AL). For the DOPC system, we fixed AL = 68, 70, 72 2; DOPC/Tat (128:2), we fixed the AL = 72, 74, 76 2; DOPC/Tat (128:4), we fixed the AL =72, 74, 76 . For each DOPC/Tat system at fixed AL, we then conducted seven independent simulations with the center of mass (COM) of each Tat constrained at different bilayer depths from the bilayer center (18, 16, 14, 12, 10, 8 and 5). In total, 45 independent simulations were conducted. The goal of constrained simulations is to find the best match between experimental and MD simulation form factors. Comparison to the X-ray form factors was performed using the SIMtoEXP software [54]. Additional details concerning the MD simulations are in Supplementary Data 6.

Chapter 3

Structural Perturbation on Lipid Bilayers Due to Tat Peptide

As discussed in chapter 2, the two main techniques employed in this thesis were molecular dynamics (MD) simulation and low angle X-ray scattering (LAXS). First, we discuss the results and analysis of diffuse X-ray scattering. The general protocol was the following; LAXS data were fitted to a model X-ray scattering pattern from a stack of flucutating membranes via NFIT program, the analysis of which yielded the bending modulus, K_C, and the bulk modulus, B. Dividing the experimenal data by the model, then, gave the absolute X-ray form factor, $|F(q_z)$, which is the Fourier transform of bilayer electron density profile along the bilayer normal direction, z. We fitted $|F(q_z)|$ to a model density profile using the scattering density profile (SDP) program. The SDP program allows us to model a bilayer density according to volumentric spacing constraint. The advantage of this program is that we can see fine details of bilayer structure such as an individual head group, terminal methly, and so on. The model requires many parameters that are not so well determined. We then constrain many parameters from the past experimental data and MD simulations. This is discussed in section ?.

The second main method is MD simulation. From simulation trajectory, we calculated the so called simulated X-ray form factor using the SIMtoEXP program (ref). The best matching simulation result was chosen as the best prediciton of the bilayer structure. We, then, calculated many structural details from the trajectory that were not accessible experimentally.

Section X discusses the implication of the results obtained in the proceeding sections. While this study does not probe dynamics of Tat translocation, it supports Tat's ability to interact with neutral membranes. This finding is compared with recent studies on a single arginine molecule.

3.1 Introduction

The name cell-penetrating peptide (CPP) connotes a peptide that easily penetrates cell membranes (for Reviews see [1-3]).

This thesis focuses on the transactivator of translation, Tat, from the HIV-1 virus, which plays a role in AIDS progression. Earlier work showed that the HIV-Tat protein (86 amino acids) was efficiently taken up by cells, and concentrations as low as 1 nM were sufficient to transactivate a reporter gene expressed from the HIV-1 promoter [4, 5]. It has been reported that Tat protein uptake does not require ATP [6]. Studies using inhibitors of different types of endocytosis, including clathrin and caveolae-mediated, or receptor-independent macropinocytosis reached the same conclusion that ATP mediated endocytosis is not involved in Tat protein permeation [7-10]. However, this issue is controversial, as other studies found evidence for endocytosis in Tat protein import [11-19]. Still other studies have concluded that an ATP requirement for Tat protein entry depends on the size of the cargo attached to Tat protein, or on the specific cell type [20-22]. The part of the Tat protein responsible for cellular uptake was assigned to a short region Tat (48-60), G48RKKRRQRRRPPQ60, which is particularly rich in basic amino acids [6]. Deletion of three out of eight positive charges in this region caused loss of its ability to translocate [6]. In this thesis, short basic regions will be called Tat, while the entire 86- amino acid protein will be called Tat protein. Tat was shown to be responsible for the Tat proteins permeation into the cell nucleus and the nucleoli [6], and this was confirmed using live cell fluorescence in SVGA cells [23]. Tat (48-60) was shown to have little toxicity on HeLa cells at 100 M concentration [6], but the longer Tat protein (2-86) was toxic to rat brain glioma cells at 1-10 M [24]. Interestingly, no hemolytic activity was found when human erythrocytes were incubated with a highly neurotoxic concentration (40 M) of Tat (2-86) [24]. These results prompt the question, what is the mechanism of Tats translocation through membranes? To address this question, many biophysical studies have used simple models of biological membranes composed of a small number of lipid types. These studies are valuable because there is no possibility for ATP-dependent translocation, thus ruling out endocytosis if translocation occurs. For example, Mishra et al. reported that the rate of entry into giant unilamellar vesicles (GUVs) composed of PS/PC (1:4 mole ratio) lipids of rhodamine-tagged Tat is immeasurably slow, but it crosses a GUV composed of PS/PC/PE (1:2:1) lipids within 30 seconds [25]. This study suggests that negative curvature induced by the inclusion of PE facilitates translocation. In a subsequent study using much smaller unilamellar vesicles (LUVs), Tat did not release an encapsulated fluorescent probe in LUVs composed of lipids modeling the outer plasma membrane, PC/PE/SM/Chol (1:1:1:1.5), but did release the probe in LUVs composed of BMP/PC/PE (77:19:4) [26]; BMP (bis(monoacylglycero)-phosphate) is an anionic lipid specific to late endosomes. In that study [26], the inclusion of PE did not suffice to cause leaky fusion in LUVs in the absence of a negatively charged lipid. The contrasting results in

9

these two experiments may also be due to the use of LUVs instead of GUVs since it was reported that Tat does not translocate across LUVS of PC/PG (3:2) but does translocate across GUVs of the same lipid composition [27]. In a similar experiment, Tat did not translocate into egg PC LUVs [28]. In another experiment confirming these results, Tat did not translocate into GUVS containing only PC with 20 mol% cholesterol, but when PS or PE was included with PC, then rapid translocation of Tat was observed [29]. These experiments demonstrate that the choice of lipids and model systems influences Tat translocation.

Is a pore formed during Tat translocation? Although direct conductance measurements of Tat and lipid membranes have not been carried out, two studies measured conductance with the somewhat similar CPP oligoarginine R9C peptide. Using single-channel conductance of gramicidin A in planar lipid membranes consisting of anionic, neutral or positively charged lipids, R9C did not increase conductance, even in anionic lipid membranes [30]. By contrast, in a similar experiment using planar lipid membranes, a current was induced by R9C in PC/PG (3:1) membranes, with increasing destabilization over time [31]. Thus questions remain about pore formation of Tat in membranes. In the GUV experiment with Tat mentioned above [29], Ciobanasu et al., using size exclusion methods, suggested a pore in the nanometer range, which could only be passed by small dye tracer molecules. Thus, if a true pore forms, it is likely to be small and transitory.

The secondary structure of Tat have been characterized by many researchers. Ref.[27] carried out Circular dichroism (CD) spectroscopy on a variation of Tat where the penultimate proline on Tat (48-60) was replaced by a tryptophan [27]. Their study found a random coil secondary structure in aqueous solution as well as when Tat was mixed with PC/PG/PE (65:35:5) LUVs. Ziegler et al.[10] obtained the same result using CD in PC/PG (3:1) vesicles. In addition, solid state NMR has identified a random coil structure of Tat in DMPC/DMPG (8:7 mole ratio) multibilayers [32]. In the larger Tat-(1-72)-protein NMR measurements at pH 4 have determined there is no secondary structure, with a dynamical basic region [33]. Similarly, NMR was used to study the full Tat protein and found a highly flexible basic region [34]. These previous studies indicate that an alpha helix is not required for Tats translocation ability.

Regarding the mechanism of translocation of this randomly structured, short basic peptide, many models have been proposed based on the conflicting results listed above. Molecular dynamics simulations offer some insight into the molecular details of translocation. Herce and Garcia simulated the translocation of Tat (Y47GRKKRRQRRR57) across DOPC at various lipid:peptide molar ratios [35]. Their simulations indicated that Tat binds to the phosphate headgroups, with 1 Tat binding with 14 lipids, each positive charge on Tat associated with nearly 2 phosphate groups [35]. Translocation involved a localized thinning, and snorkeling of arginine side chains through the hydrophobic layer to interact with phosphates on the other side of the membrane. This allowed some water molecules to penetrate the membrane

along with Tat, forming a pore [35]. In this simulation, performed without inclusion of counterions, pore formation was only observed at high ratios of peptide:lipid (1:18) or at elevated temperature. However, a subsequent Gromacs simulation with counterions found no thinning and no pore formation when Tat was added to DOPC membranes [36]. Instead it found a membrane invagination associated with a cluster of Tat peptides. From their findings, the authors suggested that micropinocytosis could be the model for Tat translocation across membranes [36].

In this work we combine experimental low-angle X-ray scattering (LAXS) data with MD simulations to obtain the structure of fully hydrated, oriented lipid bilayers with Tat (47-57) added at several mole ratios. The lipid systems were DOPC, DOPC/DOPE (3:1 mole ratio), DOPC/DOPS (3:1), DOPC/DOPE (1:1) and a mimic of the nuclear membrane (POPC/POPE/POPS/SoyPI/Chol, 69:15:2:4:11). Accessory techniques, densitometry, wideangle X-ray scattering (WAXS), neutron scattering, CD spectroscopy were also applied to further characterize Tat/membrane interactions.

3.2 Materials and Methods

3.2.1 Analysis of Diffuse Scattering

The analysis of diffuse X-ray scattering pattern begins with separating $|F(q_z)|$ from $S(\mathbf{q})$. To this end, we used an analysis program called NFIT. The derivation is described in Yufeng Liu's thesis in detail. In this section, we describe the theoretical model for $S(\mathbf{q})$ to outline the theory.

We assume that a stack of bilayers can be accurately described by the smectic liquid crystal theory, so that the free energy of the system is

$$F \tag{3.1}$$

where K_C and B are the bending and bulk modulus, respectively. Writing the membrane height profile in terms of the Fourier modes, $u = \sum \exp(i\mathbf{q} \cdot \mathbf{r})$,

$$F \tag{3.2}$$

11

3.2.2 Modeling the Bilayer Structure

In the case of X-rays, the features with the most contrast are the electron-dense headgroups, providing the head-head spacing D_{HH}, as well as the terminal methyl groups in the bilayer center. Modeling of the bilayer structure was done similarly to the SDP model [1].

Parsing of DOPC into lipid components is shown in Fig 3.1. The phosphate/choline (PC) and carbonyl/glycerol (CG) groups together make up the lipid headgroup whereas the hydrocarbon chain region is divided into two components, the methylene and methine groups combination (CH_2+CH) and terminal methyl group (CH_3). We combine methylene (CH_2) and methine groups (CH) in order to avoid proliferation of fitting parameters.

Functional forms

Our model for electron density profile (EDP) of Tat/lipid bilayer system consists of six structrual subgroups (Fig. 3.4). The volume probability distributions of components PC, CG, terminal methyl groups (CH_3), and Tat are described by Gaussian functions,

$$P_i(z) = \frac{c_i}{\sqrt{2\pi}} \left(\exp\left\{ -\frac{(z+z_i)^2}{2\sigma_i^2} \right\} + \exp\left\{ -\frac{(z-z_i)^2}{2\sigma_i^2} \right\} \right), \tag{3.3}$$

where c_i is an integrated area underneath the curve and the two parts of the expression describe the two bilayer leaflets. The calculation of c_i is explained below.

The hydrocarbon chain region (HC) is represented by error functions,

$$P_{HC}(z) = \frac{1}{2}[\text{erf}(z, -z_{HC}, \sigma_{HC}) - \text{erf}(z, z_{HC}, \sigma_{HC})], \tag{3.4}$$

where

$$\text{erf}(z, z_i, \sigma_i) = \frac{2}{\sqrt{\pi}} \int_0^{\frac{z-z_i}{\sqrt{2}\sigma}} dx \, e^{-x^2}. \tag{3.5}$$

The volume probability distribution for the methylene and methine groups combination can then be expressed as

$$P_{CH_2+CH}(z) = P_{HC}(z) - P_{CH_3}(z). \tag{3.6}$$

This definition enforces the total probability P_{HC} in the hydrocarbon chain region to equal one, which in turn means that placement of Tat in the chain region is prohibited. We call the model defined by Eq. (3.6) model A (better name?). To allow Tat to be placed inside the hydrocarbon chain region, we also consider an alternative definition,

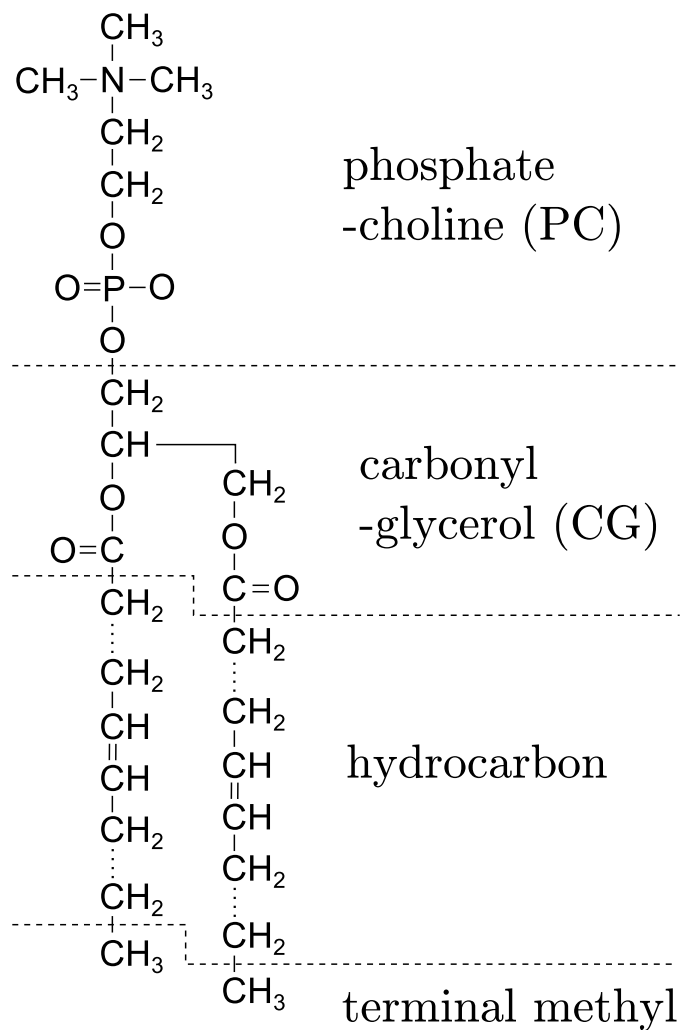$$P_{CH_2+CH}(z) = P_{HC}(z) - P_{CH_3}(z) - P_{Tat}(z), \tag{3.7}$$

Figure 3.1: Schematic of DOPC showing each lipid component. The dash lines show where the lipid is divided into different components. The lipid headgroup is divided into two components, phophate-choline and carbonyl-glycerol. The hydrocarbon chain region is also divided into two components, methelence+methine and terminal methyl groups.

where the volume probability of CH$_2$+CH combined group is reduced by the Tat volume probability distribution. We call this model model B. The spatial conservation requires the water volume probability distribution to be

$$P_{\mathrm{W}}(z) = 1 - P_{\mathrm{PC}}(z) - P_{\mathrm{CG}}(z) - P_{\mathrm{Tat}}(z) - P_{\mathrm{HC}}(z) \tag{3.8}$$

for model A and

$$P_{\mathrm{W}}(z) = 1 - P_{\mathrm{PC}}(z) - P_{\mathrm{CG}}(z) - P_{\mathrm{HC}}(z) \tag{3.9}$$

for model B.

Because X-rays measure the contrast between the bilayer and surrounding solvents, water, the experimental form factor is compared to the water subtracted model form factor,

$$F(q_z) = 2 \int_0^{\frac{D}{2}} dz \left(\sum_i (\rho_i - \rho_{\mathrm{W}}) P_i(z) \right) \cos(q_z z), \tag{3.10}$$

where $i = $ PC, CG, Tat, CH+CH$_2$, and CH$_3$.

Constraints

The height of the hydrocarbon chain error function is fixed to one by imposing spatial conservation, whereas the mean position of the terminal methyls is fixed to $z_{\mathrm{CH}_3} = 0$ by symmetry arguments. The total lipid volume V_{L} is fixed to the experimentally measured value. The headgroup volume V_{HL} was determined to be 331 Å^3 for gel phase phosphatidylcholine bilayers [2], and we assume the same volume for the fluid phase bilayers.

We define the ratios of component volumes that control volume allocation: in the headgroup region,

$$R_{\mathrm{PC}} = \frac{V_{\mathrm{PC}}}{V_{\mathrm{HL}}}, \quad R_{\mathrm{CG}} = \frac{V_{\mathrm{CG}}}{V_{\mathrm{HL}}}, \quad R_{\mathrm{Tat}} = \frac{V_{\mathrm{Tat}}}{V_{\mathrm{HL}}}, \tag{3.11}$$

and in the hydrocarbon chain region,

$$r = \frac{V_{\mathrm{CH3}}}{V_{\mathrm{CH}_2+\mathrm{CH}}}, \quad r_{12} = \frac{V_{\mathrm{Tat}}}{2 V_{\mathrm{CH}_2+\mathrm{CH}}}. \tag{3.12}$$

These volumetric parameters satisfy the following equality,

$$1 = R_{\mathrm{PC}} + R_{\mathrm{CG}} + R_{\mathrm{Tat}} \quad \text{and} \quad V_{\mathrm{L}} - V_{\mathrm{HL}} = 2 \left(16 V_{\mathrm{CH}_2+\mathrm{CH}} + r V_{\mathrm{CH}_2+\mathrm{CH}} \right). \tag{3.13}$$

14

The component volumes constraint the height of the Gaussians as

$$c_{\text{PC}} = \frac{V_{\text{PC}}}{A_{\text{L}}\sigma_{\text{PC}}} \tag{3.14}$$

$$c_{\text{CG}} = \frac{V_{\text{CG}}}{A_{\text{L}}\sigma_{\text{CG}}} \tag{3.15}$$

$$c_{\text{CH}_3} = \frac{2V_{\text{CH}_3}}{A_{\text{L}}\sigma_{\text{CH}_3}} \tag{3.16}$$

$$c_{\text{Tat}} = \frac{V_{\text{Tat}}}{A_{\text{L}}\sigma_{\text{Tat}}} \tag{3.17}$$

where A_{L} is area per lipid.

The ratio R_{CG} of the carbonyl/glycerol volume to the headgroup volume V_{HL} was suggested to be 0.41 [3], so we constrain the CG volume to 135.7 Å^3 and the phosphate/choline volume to 195.3 Å^3.

At 30 ℃, the volume of DOPC is 1303 Å^3 and the headgroup volume 331 Å^3, so the volume of hydrocarbon chain region is $1303 - 331 = 972$ Å^3 [3]. The ratio r of the volumes of the chain terminal methyl (CH$_3$) to the chain methylenes (CH$_2$) was suggested to be 1.95, and the ratio r_{12} of the volumes of the chain methines (CH) to the chain methylenes 0.91. Because there are 14 CH$_2$ groups, 2 CH groups, and 1 CH$_3$ group in each DOPC hydrocarbon chain, we have $2\times(14V_{\text{CH}_2}+2V_{\text{CH}}+V_{\text{CH}_3}) = 972$ Å^3. Using $V_{\text{CH}_3}/V_{\text{CH}_2} = 1.95$ and $V_{\text{CH}}/V_{\text{CH}_2} = 0.91$, we get $V_{\text{CH}_2} = 27.3$ Å^3, $V_{\text{CH}} = 24.9$ Å^3, and $V_{\text{CH}_3} = 53.3$ Å^3. These calculated volumes lead to $V_{\text{CH}_3}/V_{\text{CH}_2+\text{CH}} = 1.97$. At 37 ℃, the volume of DOPC was measured to be 1313.5 Å^3, so we have $2\times(16V_{\text{CH}_2+\text{CH}}+V_{\text{CH}_3}) = 1313.5 - 331$. Assuming that the ratio $V_{\text{CH}_3}/V_{\text{CH}_2+\text{CH}}$ at 37 ℃ is the same as that at 30 ℃ gives $V_{\text{CH}_2+\text{CH}} = 27.3$ Å^3 and $V_{\text{CH}_3} = 53.9$ Å^3. We constrain these volumes to the calculated values in our model.

number of e/lipid	434
volume/lipid (Å^3)	1313.5

component	n_i^e	V_i (Å^3)	ρ_i (e/Å^3)
PC	97	195.3	0.497
CG	67	135.7	0.494
CH$_2$+CH	7.875	27.3	0.288
CH$_3$	9	53.9	0.167

Table 3.1: DOPC basic structural parameters. n_i^e and ρ_i are the number of electrons and average electron density per component, respectively.

3.2.3 Volume Measurements

(Maybe do this in appendix?)

number of e/lipid	410
volume/lipid (Å^3)	1212.3

component	n_i^e	V_i (Å^3)	ρ_i ($\text{e}/\text{Å}^3$)
PE	73	94.1	0.776
CG	67	135.7	0.494
CH_2+CH	7.875	27.3	0.288
CH_3	9	53.9	0.167

Table 3.2: DOPE basic structural parameters. The notations are the same as in Table 3.1.

number of e/lipid	428
volume/lipid (Å^3)	1288.2

component	n_i^e	V_i (Å^3)	ρ_i ($\text{e}/\text{Å}^3$)
PC/PE	91	170	0.535
CG	67	135.7	0.494
CH_2+CH	7.875	27.3	0.288
CH_3	9	53.9	0.167

Table 3.3: DOPC:DOPE (3:1) basic structural parameters. The notations are the same as in Table 3.1.

number of e/Tat	838
volume/Tat (Å^3)	1877
ρ_{Tat} ($\text{e}/\text{Å}^3$)	0.446

ratio	n_{Tat}^e	V_{Tat} (Å^3)
62:1	13.6	30.5
28:1	29.5	66.1
16:1	53.0	118.8

Table 3.4: Tat basic structural parameters. The notations are the same as in Table 3.1.

	DOPC	62:1		28:1		16:1	
		A	B	A	B	A	B
V_{L}	1314	1344	1344	1380	1380	1432	1432
V_{HL}	331	362	331	397	331	450	331
V_{Tat}	0	30.5	30.5	66.1	66.1	119	119
R_{PC}	0.59	0.54	0.59	0.49	0.59	0.43	0.59
R_{CG}	0.41	0.38	0.41	0.34	0.41	0.30	0.41
R_{Tat}	0	0.08	0	0.17	0	0.27	0
r_{12}	0	0	0.558	0	1.21	0	2.17
r	1.97	1.97	1.97	1.97	1.97	1.97	1.97

Table 3.5: Volumetric constraints. A and B refer to two different models described in the text.

3.2.4 MD simulation

Three systems with different petpide concentrations (DOPC:Tat = 128:0, 128:2, and 128.4) were studied with Gromacs 4.6.1 package [4]. DOPCs were modeled by Slipid force field [5, 6] and HIV-Tats were modeled by Amber99SB [7]. The systems were simulated at 310 K with a constant area in the x-y plane. The z direction was coupled to 1 atm with constant pressure. The center of mass (COM) distance between each peptide and the bilayer was constrained by an umbrella potential with a force constant of 3000 kJ/mol/nm^2. Each system was explored 18 independent simulations as a combination of 3 different constant area and 6 different peptide insertion depths (except the pure DOPC system).

$$z_{cm} = \frac{\sum_{i=1}^{N} m_i z_i}{\sum_{i=1}^{N} m_i} \tag{3.18}$$

The center of mass constraint was applied through an external force field, which derives from an added pontential energy of the system. The pontential is like a spring, where it depends on the deviation of the distance between the center of mass of Tat and DOPC from a prefered value, z_0,

$$U(z_1^{Tat}, \ldots, z_1^{DOPC}, \ldots) = -\frac{1}{2}k\left(z_{cm}^{Tat} - z_{cm}^{DOPC} - z_0\right)^2 \tag{3.19}$$

Then, $-\partial U/\partial z_i$ is equal to the external force acting on atom, i. Before applying this constraint, Tats were attached to the bilayer from the water region. During the first 20 ns for pre-equilibration, Tats were allowed to change their configuration, which resulted in different configurations for each Tat when attached to the bilayer. It is possible that the Tats configuration inside the bilayer at the end of simulations was affected by this initial configuration of Tats. Instead of preparing many simulations with different initial Tat configurations, we avaraged over all Tats present in the system. We also performed many simulations with different A_L and z_{Tat} to investigate how robust some of the Tat structural features are. Many simulation results are shown in the appendix of this thesis.

Local Thinning of Membranes

The SIMtoEXP program only gives the average quantities for each leaflet. While our x-ray data are sensitive to the avarage bilayer electron density, local information of Tat-DOPC interactions can be obtained from MD simulations. In this section, we discuss a method to extract a local membrane thickness.

The presence of Tat may result in compression of lipid bilayer along z-direction. If so, the phosphorus-phosphorus distance of the bilayer near Tat (denoted by DPP' in the figure below) may be different from that away from Tat (DPP). For small Tat

concentration, DPP would be the same as that of pure DOPC if the distance from all Tats is large enough. Of course, for our concentrations, the thinning effect may extend throughout the bilayer because the lateral effect of Tat might have a larger lateral decay length than the distance between Tats. Whether that is the case or not, one would expect that the thickness near the Tats is smaller than the average thickness.
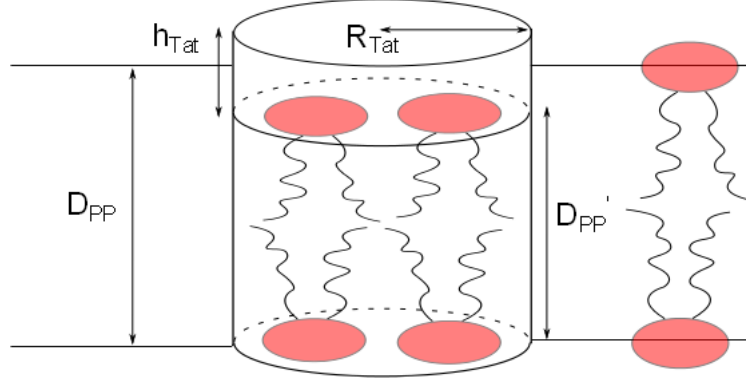

Figure 3.2: test

So, we want to measure DPP'. First, let us define what we mean by lipids close to Tat. As in Fig. 3.2, we imagine a cylinder around Tat and pick up all the phosphorus atoms within it. Approximating Tat as a cylinder with its height given by the FWHM of its electron density distribution, its radius $R_{\text{Tat}} = 9$ Å comes from the volume of Tat $= 1876$ Å^3 and $h_{\text{Tat}} = 7.6$ Å measured from one of the simulations. Let us define the lateral center of the cylinder in some way - a crude approximation would put it at the arginine in the middle of the amino acid sequence. Then let us define DPP' using only those lipids whose phosphorus atoms lie within these 9Å cylinders around the tats. Then $D_{\text{PP}} = z^+_{\text{phos}} - z^-_{\text{phos}}$ where z^+_{phos} and z^-_{phos} are the average Z of the n1 (n2) lipids in the upper and lower monolayer, respectively. To be more precise, assume that the arginine in the middle of the amino acid sequence is at the center of the cylinder. For a refined method, we could find the center of mass of each Tat and use them as the lateral center of cylinders (instead of a particular carbon atom in an arginine).

The algorithm for doing this is straightforward. For each time frame (snapshot), the positions (X_i, Y_i, Z_i) of each Tat, i, are listed. We choose phosphorus atoms whose (X, Y) lateral position lies within 9 Å of any one of the Tat's lateral position. Then, Z position of the chosen phosphorus atoms are placed in a list. Then, z_{phos} are calculated from the list. The number of selected phosphorus atoms in each monolayer was also recorded. This value gives local lateral depletion if the Tat cylinders are assumed not to overlap. After averaging over many snapshots, there will hopefully be decent statistics for local thinning and local difference between Tat and phosphorus

Z positions, and maybe local lateral depletion if overlaps are taken into account.

Linear Model

As described in the previous section, a Tat is modeled as a cylinder with its radius equal to R_1, height h_{Tat}, and volume V_{Tat} such that $R_1 = \sqrt{V_{\text{Tat}}/(\pi h_{\text{Tat}})}$. Let $h(r)$ represent the phosphorus height profile of a leaflet. The two leaflets are assumed to be decoupled. In the linear model, lipids are seprated into three regions: suppressed, boundary, and unperturbed (see Fig. for the definitions of various quantities). In the
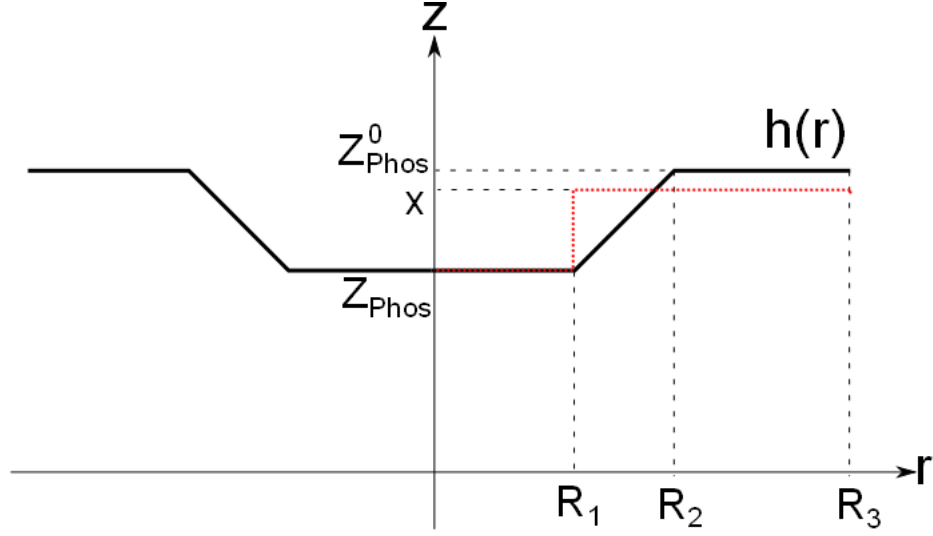

Figure 3.3: test

suppressed region, lipids are uniformly compressed by Tat toward the center of the bilayer; $h(r)$ is a constant, z_{phos}. In the boundary region, $h(r)$ is assumed to linearly increase with the distance r from the center of the Tat. In the unperturbed region, lipids do not interact with Tat, behaving identically to DOPC, so the phosphorus position is the same as that of DOPC. A continuous $h(r)$ that satisfies the above criteria is

$$h(r) = \begin{cases} z_{\text{phos}} & \text{if} \quad 0 \leq r < R_1 \\ mr + b & \text{if} \quad R_1 \leq r < R_2 \\ z_{\text{phos}}^0 & \text{if} \quad R_2 \leq r < R_3 \end{cases} \tag{3.20}$$

with $m = (z_{\text{phos}} - z_{\text{phos}}^0)/(R_1 - R_2)$ and $b = (z_{\text{phos}}^0 R_1 - z_{\text{phos}} R_2)/(R_1 - R_2)$. Assuming that the simulation box is a cylinder, we have $R_3 = \sqrt{NA_{\text{L}}/\pi}$. z_{phos} can be measured directly from simulation trajectories. z_{phos}^0 is a half of the average phosphorus-phosphorus distance in a DOPC simulation, which can be easily obtained from the SIMtoEXP program. The average height profile over the monolayer, $\langle h(r) \rangle$, can be also obtained from the program in the same manner. The only unknown is R_2, which is the relaxation length of DOPC-Tat interaction.

Let us calculate $\langle h(r) \rangle$. In the cylindrical coodinates,

$$\langle h(r) \rangle = \frac{1}{\pi R_3^2} \int_0^{2\pi} d\phi \int_0^{R_3} dr \, r h(r) \tag{3.21}$$

The ϕ integration is trivial. The r integration is

$$\int_0^{R_3} dr \, r h(r)$$
$$= \int_0^{R_1} dr \, z_{\text{phos}} r + \int_{R_1}^{R_2} dr (mr+b) r + \int_{R_2}^{R_3} dr \, z_{\text{phos}}^0 r$$
$$= \frac{1}{2} \left[z_{\text{phos}} R_1^2 + z_{\text{phos}}^0 (R_3^2 - R_2^2) \right] + \frac{1}{3} m \left(R_2^3 - R_1^3 \right) + \frac{1}{2} b \left(R_2^2 - R_1^2 \right)$$
$$= \frac{1}{2} \left[z_{\text{phos}} R_1^2 + z_{\text{phos}}^0 (R_3^2 - R_2^2) \right] + \frac{1}{3} \left(z_{\text{phos}}^0 - z_{\text{phos}} \right) \left(R_2^2 + R_1 R_2 + R_1^2 \right)$$
$$+ \frac{1}{2} \left(z_{\text{phos}} R_2 - z_{\text{phos}}^0 R_1 \right) (R_1 + R_2) \tag{3.22}$$

Using Eq. (3.22), we get

$$\langle h(r) \rangle = \frac{\left(z_{\text{phos}} - z_{\text{phos}}^0 \right) \left(R_1^2 + R_1 R_2 + R_2^2 \right) + 3 z_{\text{phos}}^0 R_3^2}{3 R_3^2} \tag{3.23}$$

Eq. 3.23 is a quadratic equation in terms of R_2. Solving for R_2 gives

$$R_2 = \frac{-R_1 + \sqrt{R_1^2 + 4C}}{2} \tag{3.24}$$

with

$$C = \frac{3 R_3^2 \left(z_{\text{phos}}^0 - \langle h(r) \rangle \right)}{z_{\text{phos}}^0 - z_{\text{phos}}} - R_1^2 \tag{3.25}$$

The model quantities calculated from the MD simulations are shown in Table.

3.3 Results

3.3.1 Material Elasticity Parameters

Show X-ray data. Show fitting boxes. Show the Kc values. Also, show the resultant form factors, which qualitatively show the membrane thinning. Fig. XX shows the scattering intensity pattern from DOPC/DOPE (1:1) with mole fraction x=0.034 Tat. The diffuse lobes are due to equilibrium fluctuations that occur in these fully hydrated, oriented lipid/peptide samples. The intensity $I(q)$ in the diffuse patterns provide the absolute values of the form factors $F(q_z)$, which are the Fourier transforms of the electron density profile, through the relation $I(\mathbf{q}) = S(\mathbf{q}) |F(q_z)|2/q_z$, where $q = (q_r, q_z)$,

$S(q)$ is the structure interference factor, and q_z^1 is the usual LAXS approximation to the Lorentz factor [39, 55, 56]. The first step in the analysis takes advantage of the q_r dependence of the scattering to obtain the bending modulus K_C with results shown in Fig. 2. As positively charged Tat concentration was increased, the lamellar repeat spacing D generally increased in neutral lipid bilayers and decreased in negatively charged bilayers, consistent with changes in electrostatic repulsive interactions. With few exceptions, the water space between bilayers exceeded 20 Å.

The analysis that obtains K_C also obtains the structure factor $S(\mathbf{q})$ and then the unsigned form factors $|F(q_z)|$ are obtained from the intensity $I(q)$ by division. Results for five different membrane mimics are shown in Fig. 3. Vertical lines indicate the zero position between the lobes of diffuse data where $F(qz)$ change sign. In every sample, the zero positions shift to larger q_z, indicating a thinning of the membranes.

3.3.2 Volume results

Experimental and simulated volumes are given in Table 2. The simulated volume was obtained using the volume app in the SIMtoEXP program. The experimental Tat volume was calculated from the measured density assuming that the lipid volume was the same as with no Tat. In general, there may be an interaction volume between the peptide and the lipid membrane as we found previously for bacteriorhodopsin [57]. As lipid was present in excess to Tat, the partial molecular volume of the lipid should be the same as with no Tat, so this way of calculating includes all the interaction volume in VTat. Comparison of VTat in water with the result for 5:1 Lipid:Tat suggests that the interaction volume may be negative, consistent with a net attractive interaction with lipid. Understandably, values of VTat were unreliable for small mole ratios of Tat:Lipid. Therefore we used simple additivity for those mimics not shown in Table 2 for the volumes used in the SDP program. All volumes obtained from the Gromacs MD simulations were somewhat smaller than the measured volumes, but it supports the Tat volume being closer to 1822 3 than the outlying values obtained experimentally at small Tat concentrations.

3.3.3 Scattering Density Profile Modeling

Using the model described above, we fitted our measured X-ray form factors. The positions of componet groups were free parameters the agreement with the experimental form factors was excellent. Figure 3.5 shows that the best fit to the DOPC form factor was very good. Figure 3.4 shows the model electron density profile derived from the best fit. (Table ? shows the best fit parameters for DOPC bilayers. Explain the constraints on the distance between the headgroup components.)

For fitting the form factors for systems with Tat, we fixed the width of Tat Gaussian because we found that the best fits of this width was always unphysically too small. We fitted with three different values of widths, 2.5, 3.0, and 3.5, to study
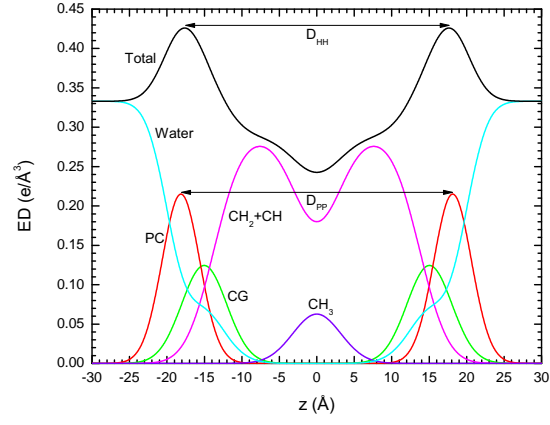
Figure 3.4: DOPC electron density (ED) profile
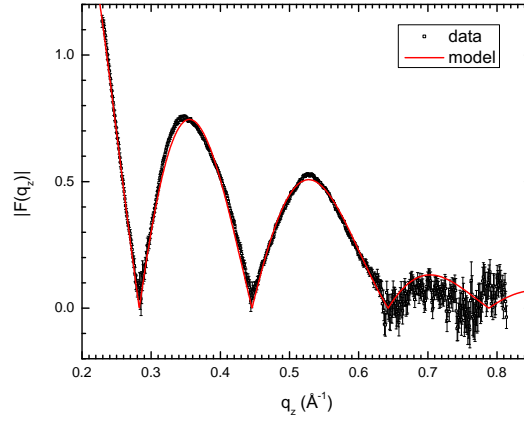
Figure 3.5: DOPC form factor

the range of variation due to the Tat width. The choice was made based on MD simulation results. (Check this again) Figure 3.6 shows the best fit to the form factor for DOPC:Tat (62:1). (Show all the results in a composite figure. Show results for
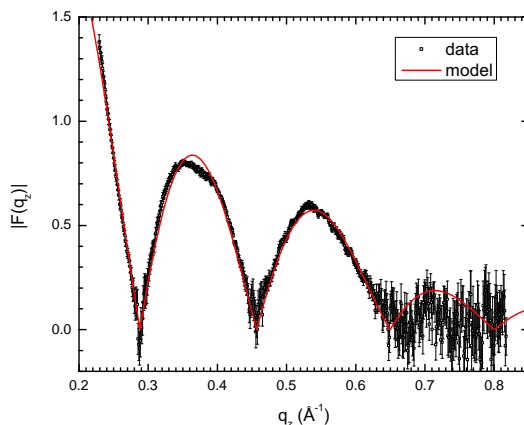
Figure 3.6: DOPC:Tat (62:1) form factor
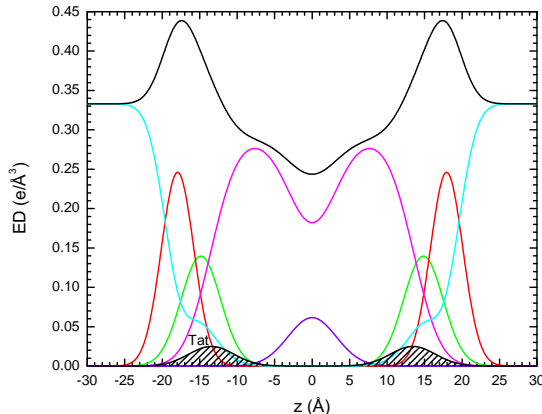
Figure 3.7: DOPC:Tat (62:1) ED profile. Colors are the same as in Fig. 3.4

DOPC:DOPE bilayers.)

Figure 3.8 shows χ^2 as a function of fixed Tat position, z_{Tat}. Generally, two minima were found. For DOPC bilayers, z_{Tat} in the headgroup region yielded the best fit. (Show plots for DOPC bilayers) However, as Fig. 3.9 shows, the fits are are equally good with Tat inside and outside the chain region for DOPC:DOPE bilayers. (Show a bunch more plots for DOPC:DOPE membranes) While modeling suggested that Tat could be in the tail region, this position seems energetically unfavorable as Tat is

23
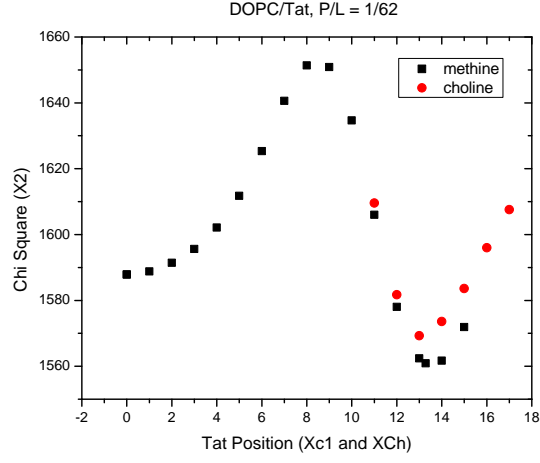
Figure 3.8: χ^2 as a function of z_{Tat} for DOPC:Tat (62:1).
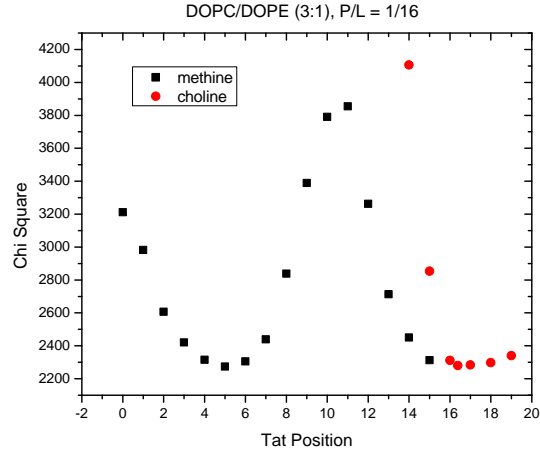
Figure 3.9: χ^2 as a function of z_{Tat} for DOPC:DOPE (3:1) with $x_{\text{Tat}} = 1/17$, where $x_{\text{Tat}} = Tat/(Tat + Lipid)$.

a hydrophilic molecule. With a help of MD simulations, we were able to discard the interior position as an artifact of our modeling. The simulation results are discussed later.

It must be emphasized, however, that, while the total EDP is well determined by this fitting procedure, the values of the parameters for the components are not as well determined as the agreement of the fit to the data may suggest. Indeed, we found local minima in the fitting landscape, including one with Tat closer to the center of the bilayer as shown in Fig. S5. The simulations help to discard that result. Electron density profiles for DOPC/DOPS (3:1) and the nuclear membrane mimic were not successful, due to loss of diffuse scattering by Tats charge neutralization of these negatively charged membranes.

More structural detail from the modeling and from the simulations is shown in Fig. 7. The bilayer thickness can be described as DHH, which is the distance between the maxima in the electron density profile, or as DPP, which is the distance between the phosphocholines on the opposing monolayers (see Fig. 5). Figs. 7A and 7B show that both these quantities tend to decrease with increasing Tat mole fraction (P/(L+P)), showing that Tat thins membranes, increasingly so as its concentration is increased, even though both simulation and modeling suggest that Tat moves further from the membrane center with increasing concentration as shown in Fig. 7D. Fig. 7C shows that the area per lipid AL usually increases with increasing mole fraction of Tat, similar to the findings from MD simulations (Section 3.2), as would be expected. The results from the simulation data plotted in Fig. 7 were obtained by using a weighted average based on chi-square of the four best fits of the simulated form factors with the experimental form factors.

Figure shows that A_L as defined by $(V_L - V_{HL})/D_c$ decreases as the amount of DOPE increases for systems without Tat. This is consistent with the previous studies (or predictions?) and attributed to the small size of PE head group. Because DOPE has smaller head group than DOPC, lipids in DOPC/DOPE bilayers pack more compactly than DOPC bilayers do, leading to a smaller A_L. Consequently, bilayers composed of DOPC and DOPE tend to have a higher order parameter than DOPC alone. (NO THEY DON'T. WHAT'S GOING ON HERE?). Similarly, the thickness of bilayers is larger at higher PE content.

Figure shows that Tat is located further out from the bilayer center with higher content of PE lipids. This is also consistent with MD simulation PMF, which showed that arginine insertion cost more energy for PE membrane than PC membrane, the result of which was attributed to more possible hydrogen bonding between PE group and arginines.

More structural detail from the modeling and from the simulations is shown in Fig. 7. The bilayer thickness can be described as DHH, which is the distance between the maxima in the electron density profile, or as DPP, which is the distance between the phosphocholines on the opposing monolayers. Figs. 7A and 7B show that both these quantities decrease with increasing Tat mole fraction (P/(L+P)), showing that

Tat thins membranes, increasingly so as its concentration is increased, even though both simulation and modeling suggest that Tat moves further from the membrane center with increasing concentration as shown in Fig. 7D. Fig. 7C shows that the area per lipid AL usually increases with increasing mole fraction of Tat, as would be expected from consideration of conservation of lipid volume. Interestingly, the bilayer thickness did not increase for DOPC/DOPE (3:1) bilayers with x less than 0.03.

3.3.4 Molecular Dynamics Simulations

Due to the slow relaxation in lipid bilayers and limited accuracy of the force field, a good agreement between experimental and MD simulation calculated form factors may be difficult to reach. Consequently, we carried out several constrained simulations at A_L and Z_{Tat} as described in Materials and Methods. We then compared the simulated form factor $F(q_z)$ with the experiment. The best match for DOPC/Tat (128:4) was found when the Tats were constrained at 18 Åaway from the bilayer center (Fig. 4.A,B). The other best fit results were: DOPC $A_L = 70$ $\mathring{A}^2$ and DOPC/Tat(128:2) A_L = 72 $\mathring{A}^2$, $Z_{Tat} = 18\mathring{A}$. It clearly indicates that with increasing Tat concentration, A_L increases. The agreement worsened as Tat was constrained to be closer to the center of the bilayer. When Tats were constrained at 5 Åaway from the bilayer center, we observed a spontaneous formation of water pores in the MD simulation. However, as shown in Fig. 4.C the corresponding form factor calculated from MD simulations does not match well with experiments. Figure 4. MD simulated form factors (red solid lines in A and C) of Tat/(DOPC+Tat), x=0.030, with Tat fixed at ZTat= 18 (panel A) and 5 (panel C) from the bilayer center compared to experimental form factors (open circles) scaled vertically to provide the best fit to the simulations. Corresponding snapshots are shown in Panels B and D in which the lipid chains are represented as grey sticks on a white background, Tats are yellow, phosphate groups are red and water is blue.

3.3.5 Summary of Results

We summarize our results for how Tat affects the lipid bilayer in Fig. 9. The height of Tat, $H_{Tat} = 8.7\mathring{A}$, was the full width at half maximum of the Tat electron density profiles obtained from simulations and the cylindrical radius, $R_{Tat} = 8.3\mathring{A}$, was calculated to give the measured volume. The Z distances from the center of the bilayer were derived from weighted averages of four MD simulations of Tat:DOPC 2:128. The χ^2 obtained by comparison to experiment indicated that the best Z_{Tat} lay between the simulated values of 16 Åand 18 Åand the best area/lipid A_L lay between the simulated values of 72 $\mathring{A}^2$ and 74 $\mathring{A}^2$, so averages were obtained from these four combinations of Z_{Tat} and A_L, weighted inversely with their χ^2. The average positions, Z'Phos, of phosphates situated underneath the Tats were calculated by averaging over the phosphates whose in-plane distance, R, from the center of Tat

is smaller than RTat. The simulation cell extended to 38, far enough to ensure that ZPhos for most of the lipids is the same as for DOPC. Assuming a simple linear ramp in ZPhos, Fig. 9 then indicates a ring of boundary lipids that extends twice are far in R as Tat itself. Although the guanidinium electron density profile was broad (Fig. S8), indicating that some were pointing away from the bilayer relative to the center of Tat, more were pointing towards the bilayer center as indicated in Fig. 9. Numerical values are given in Table S1.

3.4 Discussion

Given that 8 of the 11 amino acids in Tat (47-57) are arginines and lysines, one would have suggested 20 years ago that highly charged Tat would partition strongly into solution rather than being associated with lipid bilayers. By contrast, but in agreement with more recent perspectives on arginine partitioning into the interfacial region [58], we find that Tat interacts with lipid bilayers, even with neutral DOPC and DOPC/DOPE mixtures, as well as with negatively charged DOPC/DOPS and nuclear membrane mimic lipid mixtures. This paper presents multiple lines of evidence for a Tat/membrane interaction. Fig. 2 shows that Tat decreases the bending modulus. Although one could argue that such a decrease is only apparent and could instead be due to local changes in membrane spontaneous curvature [59], either interpretation supports a Tat-bilayer interaction. The changes with increasing Tat concentration in the X-ray membrane form factors in Fig. 3 prove that Tat affects membrane structure, and the shift of the zero positions to higher q_z suggests thinning. Thinning is substantiated by quantitative analysis of the X-ray data and by MD simulations. Fig. 7A shows that the average membrane thickness, as measured by the distance DPP between phosphocholines on opposite surfaces, decreases with increasing Tat concentration. Similar thinning is shown in Fig. 7B for the distance DHH between the maxima in the electron density profiles of opposite surfaces. Compared to DPP, DHH is pulled towards both the carbonyl/glycerol groups and Tat because both have electron densities (0.4 e/3) greater than water (0.33 e/3) or hydrocarbon (0.3 e/3). Although the thinning shown in Figs. 7A and 7B is not large, it obviously requires interaction of Tat with the bilayers. Fig. 7C shows that AL increases with increasing Tat concentration, by both model fitting and MD simulations.

It is of considerable interest to learn where Tat resides, on average, in the membrane, as this would establish a base position from which translocation would be initiated. We have combined our two main methods, MD simulations and X-ray scattering, to address this question. In general, Tats locate at the bilayer/water interface as indicated in Section 3.2, and they are close to the phosphocholine headgroup region by comparing the simulated 2ZTat in Fig. 7.D with 7.A. Although the SDP modeling of the X-ray data obtains excellent fits to the experimental form factors for a model with Tat deep in the hydrocarbon interior (see Fig. S5), the corresponding MD simulation (shown in Fig. 4.C) eliminates this spurious result. Fig. 7D also shows

that modeling gives smaller values for ZTat than the simulation. The modeling result is supportive of the original simulation result of Herce and Garcia that Tat resides closer to the bilayer center than do the phosphocholine groups [60]. That is a base position that would be a possibly important precursor to translocation, as would the larger AL.

Several groups have carried out calculations and MD simulations showing that the cost of moving an arginine group from water to the bilayer center is 12-26 kcal/mol [58, 61-63] or 6-7 kcal/mol if side-chain snorkeling to the surface is taken into account [64]. This is not inconsistent with our result that Tat interacts with the membrane because, as is well known, the bilayer is not just a hydrocarbon slab, but has interfacial headgroup regions where Tat can reside. It has been suggested that the free energy cost for charged amino acids entering the headgroup region is similar to that for partitioning into octanol, about an order of magnitude smaller free energy cost than partitioning into cyclohexane [65-67]. Simulations suggest that the free energy is smaller for an arginine residing in the interfacial region than in water, roughly by 3 kcal/mole, depending upon the lipid [58, 67]. Our results therefore appear energetically reasonable.

One concern with diffraction experiments on samples consisting of adjacent bilayers in a stack or in a multilamellar vesicle is that the samples have to be partially dried to obtain conventional diffraction data. But then there is no pure water layer between adjacent bilayers, so a hydrophilic peptide is forced into the interfacial, partially hydrophilic region of the lipid bilayer. In contrast, by using diffuse scattering, we obtained structure from experimental samples that had a range of lamellar D spacings (see Fig. 2 caption) that were considerably larger than the thickness of the bilayer in Fig. 7A, thereby providing an ample pure water space, typically greater than 20. The result that 2ZTat shown in Fig. 7D is so much smaller than our repeat spacings shows that Tat preferentially associates with the membrane rather than dissociating into water.

Consistent with Tat softening the bilayers (Fig. 2), it also disorders them as indicated by Sxray decreasing with Tat concentration shown in Fig. 8. Tat also increases the mosaic spread observed by X-ray and neutron scattering as shown in Figs. S1-3; this is a much larger scale disordering of the stack of bilayers. As shown in Table 1 and in Fig. S7, Tat assumed slightly ¿50membrane. Our results were determined using the DichroWEB program, which compares the mean residue ellipticity with that from standard globular proteins, with details given in Supplementary data near Fig. S7. These structures include approximately equal amounts of regular strands and turns, with half that amount of distorted strands. The next most prevalent structure was random coil (37Introduction) report a primarily random structure, determined using either CD or NMR. This difference could be due to different sample preparations, or due to a different interpretation of the CD spectra. Ref. [68] reported that CD spectra of unordered polypeptides are similar to that of the poly(Pro)II helix, and a significant fraction of the unordered conformation in globular proteins consists of

poly(Pro)II helix plus distorted strands.

In an effort to better determine the secondary structure of Tat, our collaborator, Dr. Rieko Ishima, performed 1D and 2D-NMR of Tat in solution at 10, 20 and 30oC. Her results showed no evidence for backbone hydrogen bond formation, indicating that the peptide does not have a stable conformation, at least on the time scale of the NMR measurement. Additionally, we analyzed the secondary structures of Tats from MD simulations using the Define Secondary Structure of Proteins (DSSP) program [69]. Data from the MD simulation which has the best fit to experimental X-ray form factors show that Tat contains neither nor -helix structures. Therefore, both our solution NMR and MD simulation results find primarily random coil, with no significant structure, which contrasts with our CD findings of ¿50the interpretation of CD spectra as , P2 helix or coil is controversial, what is clear is that the membrane does not influence the conformation of solubilized Tat. In addition, no studies including our own, have implicated Tat forming an -helix, either in solution or in the membrane.

Given our structural and elastic moduli results, we now compare to other experiments in the literature. In 2008, the Wong group implicated Tats ability to induce saddle-splay curvature with a potential role of bidentate hydrogen bonding as key [70]. Rhodamine-tagged Tat only entered GUVs when the PE headgroup was included with PS and PC lipids (PS/PC/PE, 20:40:40), indicating that hydrogen-bonding, and/or curvature-promoting lipids are required for Tat translocation. In PS/PE (20:80) lipids, they found Tat caused a highly curved cubic phase using X-ray diffraction [70]. In our experiments, there was little effect of adding DOPE to DOPC at either a 3:1 or 1:1 mole ratio on decrease in the bending modulus, bilayer thinning, Tats outward movement with increasing concentration or disordering of chains (Sxray). Our two results are not inconsistent, however, since curvature-promotion appears not to be required for Tats ability to lower the energy required to bend, nor to locate Tat in the bilayer, nor to disorder chains, all of which may be important for Tat translocation. Yet Tat does translocate across membranes in their experiments only with PE in the membrane, so the ability to induce saddle- splay curvature may also be required for Tats translocation. Another study by Melikov et al. [26] found that Tats main mechanism of action is to induce lipid mixing and membrane leakage with lipids of late endosomes. This result is consistent with our results that Tat induced a reversible, hydration-induced increase in mosaic spread (Figs. S1-3) and a disordering of chains (Fig. 8). Both of these could induce lipid mixing and perhaps, membrane leakage. An X-ray, neutron and AFM study reported thickening upon initial Tat binding, in contradiction to our result in Fig. 7B that shows thinning [71]. We suggest that this difference was caused by their using stiff gel phase DPPC lipid that did not allow bound Tat to perturb the bilayer. Using a variety of techniques, including high sensitivity isothermal titration calorimetry and 2H- and 31P- NMR, Seelig et al. [72] presented evidence that the lipid bilayer remains intact upon Tat binding and our results confirm this. Finally, we compare our structural results to

those obtained by solid state NMR, although at a lower hydration level than in our sample. Hong et al. [32] found that Tat lies parallel to the bilayer surface in the headgroup region of DMPC/DMPG (8:7) bilayers, similar to our cartoon in Fig. 9.

3.5 Conclusion

Although a recent MD simulation using umbrella sampling [73] found that the free energy required for cR9 to traverse a membrane was smaller if a water pore was present, we cannot directly test the existence of a transient water pore from our X-ray or neutron scattering experiments. This is because, even with a water pore, the translocation process still requires crossing a free energy barrier which is a non-equilibrium process. X-ray form factors measure an equilibrium state. If the form factors obtained from water pore structures agreed well with experiments, it would indicate that the pore structure was thermodynamically stable. This may be the case for some antimicrobial peptides, but certainly not for cell-penetrating peptides. Finding a kinetically competent pathway for the interesting phenomenon of translocation of highly charged Tat through hydrophobic membranes is difficult. An energetically passive translocation likely occurs very seldom on an MD simulation time scale, and it probably happens quickly, so it would not significantly change the average structure of the membrane in which it occurs. Although our results in this paper do not reveal a kinetically competent pathway, they do show that Tat is drawn to the surface of the membrane, and is therefore ready for translocation at a region of local thinning. And they show that these interactions tend to soften (Fig. 2) and disorder (Fig. 8) the membrane and increase the AL, thereby likely reducing the energy barrier for passive translocation.

Chapter 4

Ripple Phase

When the temperature is reduced from the fluid phase, the ripple phase is observed in bilayers consisting of fully saturated lipids. This chapter discusses X-ray scattering experiments on the ripple phase formed by dimyristolphosphatydylcholine (DMPC) bilayers.

4.1 Introduction

The ripple phase is the greatest thermodynamic phase of lipid bilayers. This phase was originally found by Tardiue et al. in some lipid bilayers. What did they find? Further work on the ripple?

The structure of the ripple phase bilayers can be divided into two categories: 1) the average electron density profile that characterizes how each bilayer is packed within a stack of lipid bilayers and 2) lateral lipid structure that characterizes how lipid chains are packed.

Extensive work was done by Wack and Webb (1989). The X-ray form factor for DMPC was analyzed by Sun et al. Sengupta et al studied the temperature dependence of DMPC and other lipids.

Hatchel (1991) did wide angle scattering (transmission) for DPPC. Rughnathan and Katsaras did near grazing angle WAXS on DMPC. Sengupta et al. suggested lipid chain packing in 2003 based on average bilayer electron density (ED) profile calculated from low angle X-ray scattering. de Vrie et al suggested interdigitated chain in the minor side based on molecular dynamics (MD) simulations.

Many theoretical work have been done to understand the origin of the ripple phase. Some work include Lubensky and Macintosh, ...

These theories predict chain packing in both major and minor sides. It is obviously important to determine the packing in order to validate or invalidate those theories. However, this information is not completely known. WAXS is a direct probe of the chain packing. It is difficult because scattering is rather weak compared to gel phase.

Here, we report DMPC average structure calculated from low angle X-ray scattering data collected at a synchrotron. Careful analysis allowed us to derive a high resolution ED profile. The profile suggests WHAT?

We also report wide angle X-ray scattering, and suggest chain packing based on both LAXS and WAXS. Highly brilliant synchrotron X-ray allows high resolution study on weak, possibly diffuse scattering. We determined that the peak is off the equator and tilted from the virtical q_z axis.

4.2 Materials and Methods

High resolution was achieved by the use of Germanium monochromator, 0.01% energy dispersion. Low resolution data were taken with multilayer monochromator with 1% energy dispersion.

To achieve small mosaic spread, samples were annealed at 60 ℃for at least 6 hours right before the experiment. Silicon wafers were cleaned just before use. 2:1 methanol: chloroform was used to dissolve DMPC. Sample were rocked continuously during solvent evaporation and dried further inside a glove box. Samples were then dried under a hood for 24 hours and in a vaccume chamber for 2 hours. Samples were stored in a refrigerator.

A thin piece of molybdenum was used to attenuate the beam. The attenuation length μ of X-ray in Mo is 6.433 μm for 8 keV and 13.74 μm for 10.55 keV [8]. For a nominal 25 μm thick Mo attenuator, $\mu = 13.74$ gives the attenuation factor of $[\exp(-25/13.74)]^{-1} = 6.2$. The exact attenuation factor was determined by taking images with and without the attenuator and calculating a factor that needed to be multiplied for the images to match with each other.

Low angle scattering was done with low resolution setup.

25 μm silicon wafer was used to deposit our sample. This wafer absorbs only 20% of the X-ray beam at 10.5 keV (Check this). This weak absorption allows transmission scattering. Trasmission experiment was done with low resolution setup.

Grazing angle experiment was done with both high and low resolution setups. To minimize geometric broadening in grazing angle experiment, the sample was trimmed to either 1 or 2 mm.

4.2.1 Sample Preparation

DMPC was purchased from Avanti Polar Lipids and used without further purification. Oriented thin film was deposited following the rock and roll procedure. In previous synchtrotron experiments, the samples were created and annealed more than a week in advance and stored in a refrigerator. The orientation quality of these samples were found to be worse than the quality soon after the samples were annealed. Therefore, to ensure the best sample quality, the sample was annealed for approximately 12 hours just before the X-ray experiment. Figure X compares a sample scattering in

2011 and 2013 synchrotron runs. Because of substantial degree of mosaic spread in the 2011 sample, many peaks overlapped, rendering the accurate measurement of integrated intensity difficult. Figure XX shows a picture of the annealing chamber. To achieve gentle but efficient hydration of a sample, filter papers were installed to cover the sample. For successful annealing, it must be emphasized that the annealing chamber equilibrates in the over prior to putting the samples in the chamber. When the sample was put in the chamber with its water at room temperature and then the system was placed inside the oven, warm vapor condensed on the cooler sample, causing so called flooding of oriented sample. A small drop of water on the oriented film was deterimental for the orientation because the bilayers tend to peel off, resulting in entropy-driven formation of unoriented vesicles in the water subphase.

The sample for grazing incident wide angle study was prepared in the same way as for low angle study. In order to minimize the geometric broadening, the sample was further trimmed down to 1 mm in width.

The sample for transmission study was deposited on a thin, 35 micron, silicon wafer. Because the wafer was very fragile, attaching the sample to a sticky thing was impossible. Instead, the sample was attached to a plastic cap of a small vial with a small amount of heat sink compound at a conrner of the wafer. The wafer was stable enough for rocking. The sample deposited on a glass cover slip (70 microns) was prepared similarly.

4.2.2 Low Angle Diffraction Experiment

The same setup as described in Tat chapter was used for low angle diffraction experiment. In order to achieve a D-spacing comparable to that of Wack and Webb ($D \approx 57.9$ Å), the current to the Peltier was reversed, which heats the Peltier surface the sample was situated on.

The integrated intensity of each peak was obtained by putting a box around a peak and summing up the intensity in those pixels that fall inside the box. The background scattering was estimated by measuring the intensity in pixels near the peak but not containing any peak tail. The choice of box side was made according to the width of each peak. Because of mosaic spread in the sameple, peaks were wider for higher orders. Accordingly, the box was made wider for higher orders. The box size was chosen so that approximately 90% of the peak intensity was counted toward the integrated intensity.

A few peaks in the ripple phase were very strong, leading to saturation of CCD pixels. A nominally 25 micron molybdinum attenuator was inserted in the upstream to reduce the intensity of the X-ray beam and one second exposure was collected. The integrated intensity of the most strong, (1,0) peak was measured from this short exposure. To measure the actual attenuation factor, a one second exposure without the attenuator was also taken. Comparison of these two images yielded an attenuation factor of 7.8. The intensity of (2,0) and (2,-1) peaks were also measured in this one

second exposure with an attenuator. All the other peaks were observed without saturation in 60 second exposure. To properly scale the strong orders, (1,0) peak intensity was multipied by 7.8 x 60 and (2,0) and (2,-1) were multiplied by 60.

The integrated intensity, peak position in pixel, the size of box, and estimated background for all the peaks are shown in Appendix.

4.2.3 Near Grazing Angle Experiment

Plot along the peak, along the arc, horizontal, vertical, etc.

4.2.4 Transmission Experiment

No strong order on the equator. Subtraction of water scattering from the background image.

4.2.5 Model

4.3 Lattice Structure

It has been shown from X-ray studies (ref) that ripples in in different bilayers are registered to form a two-dimensional oblique lattice as shown by the unit cell in Fig. X. The unit cell vectors in the ripple phase can be expressed as

$$\mathbf{a} = \frac{D}{\tan\gamma}\hat{\mathbf{x}} + D\hat{\mathbf{z}} \tag{4.1}$$

and

$$\mathbf{b} = \lambda_r\hat{\mathbf{x}}. \tag{4.2}$$

The corresponding reciprocal lattice unit cell vectors are

$$\mathbf{A} = \frac{2\pi}{D}\hat{\mathbf{z}} \tag{4.3}$$

and

$$\mathbf{B} = \frac{2\pi}{\lambda_r}\hat{\mathbf{x}} - \frac{2\pi}{\lambda_r\tan\gamma}\hat{\mathbf{z}}. \tag{4.4}$$

The reciprocal lattice vector, $\mathbf{q}_{hk}$ for the Bragg peak with Miller indices (h, k) is

$$\mathbf{q}_{hk} = h\mathbf{A} + k\mathbf{B}, \tag{4.5}$$

so its Cartesian components are

$$q_k^x \equiv q_{hk}^x = \frac{2\pi k}{\lambda_r} \tag{4.6}$$

$$q_{hk}^y = 0 \tag{4.7}$$

$$q_{hk}^z = \frac{2\pi h}{D} - \frac{2\pi k}{\lambda_r\tan\gamma}. \tag{4.8}$$

4.4 Scattering Basics

The incoming and outgoing wavevectors of the x-ray beam in Fig. XXX are given by

$$\mathbf{k}_{\text{in}} = \frac{2\pi}{\lambda}\hat{\mathbf{y}}, \quad \mathbf{k}_{\text{out}} = \frac{2\pi}{\lambda}\left(\sin 2\theta \cos \phi\, \hat{\mathbf{x}} + \cos 2\theta\, \hat{\mathbf{y}} + \sin 2\theta \sin \phi\, \hat{\mathbf{z}}\right), \qquad (4.9)$$

where λ is the wavelength of x-ray, 2θ is the total scattering angle, and ϕ is the angle measured from the equator on the detector. The scattering vector (also called momentum transfer vector) is the difference between $\mathbf{k}_{\text{in}}$ and $\mathbf{k}_{\text{out}}$,

$$\begin{aligned} \mathbf{q} &= \mathbf{k}_{\text{out}} - \mathbf{k}_{\text{in}} \\ &= q\left(\cos\theta \cos\phi\, \hat{\mathbf{x}} - \sin\theta\, \hat{\mathbf{y}} + \cos\theta \sin\phi\, \hat{\mathbf{z}}\right), \end{aligned} \qquad (4.10)$$

where $q = 4\pi \sin\theta/\lambda$ is the magnitude of the scattering vector. When the sample is rotated by ω about the lab x-axis in the clockwise direction as shown in Fig. XXX, the sample q-space also rotates and are given by

$$\hat{\mathbf{e}}_{\mathbf{x}} = \hat{\mathbf{x}}, \quad \hat{\mathbf{e}}_{\mathbf{y}} = \cos\omega\, \hat{\mathbf{y}} + \sin\omega\, \hat{\mathbf{z}}, \quad \hat{\mathbf{e}}_{\mathbf{z}} = -\sin\omega\, \hat{\mathbf{y}} + \cos\omega\, \hat{\mathbf{z}}. \qquad (4.11)$$

From Eq. (4.10) and (4.11), we find the sample q-space to be

$$\begin{aligned} q^x &= \mathbf{q} \cdot \hat{\mathbf{e}}_{\mathbf{x}} = q\cos\theta\cos\phi, \\ q^y &= \mathbf{q} \cdot \hat{\mathbf{e}}_{\mathbf{y}} = q\left(-\sin\theta\cos\omega + \cos\theta\sin\phi\sin\omega\right), \\ q^z &= \mathbf{q} \cdot \hat{\mathbf{e}}_{\mathbf{z}} = q\left(\sin\theta\sin\omega + \cos\theta\sin\phi\cos\omega\right). \end{aligned} \qquad (4.12)$$

The position, (X, Z), of a CCD pixel is measured with respect to the beam and given by

$$X = S\tan 2\theta \cos\phi, \quad Z = S\tan 2\theta \sin\phi, \qquad (4.13)$$

where S is the distance between the sample and detector. From a model for the electron density of a lipid bilayer, one calculates a X-ray scattering intensity pattern, $I(\mathbf{q})$. Then, Eq. (4.12) and (4.13) relate $I(\mathbf{q})$ to the experimentally measured intensity pattern, $I(X, Z)$. It is important to remember that a given pixel position, (X, Z), corresponds to a triplet (q_x, q_y, q_z). Fully exploring the sample q-space requires changing ω for a fixed wavelength, which was achieved by continuously rotating the sample with a motor. In the ripple phase, because our sample has in-plane rotational symmetry, the ripple side peaks make up Bragg rings while the main peaks are still delta function like (see Fig. X) in q-space. In order for the main peak to be observed, ω must be equal to θ_{B}, but the side peaks are observed at any ω. Those side peaks get slightly smeared due to integration over q_y.

For low angle x-ray scattering (LAXS), it is convenient to linearize the above equations in terms of θ and ω. In the small angle approximation, $\sin\phi \approx Z/(2S\theta)$

and $\cos\phi \approx X/(2S\theta)$, and

$$q_x \approx \frac{4\pi\theta\cos\phi}{\lambda} \approx kX/S$$

$$q_y \approx q_z\omega - \frac{4\pi\theta^2}{\lambda} \approx q_z\omega - \frac{\lambda q_z^2}{4\pi}$$

$$q_z \approx \frac{4\pi\theta\sin\phi}{\lambda} \approx kZ/S, \tag{4.14}$$

with $k = 2\pi/\lambda$. For wide angle X-ray scattering, the exact relations given by Eq. (4.12) are necessary. Especially in the transmission experiment, where ω is large, an observed X-ray pattern appears nontrivial and becomes almost impossible to analyze without the use of Eq. (4.12).

4.5 Geometric (Lorentz) Correction for Ripple Phase Scattering

Our sample has in-plane rotational symmetry. This means that the sample consists of many domains with differing ripple directions, all domains being parallel to the substrate. In sample q-space, then, ripple side peaks become rings while main peaks are still points (see Fig. X). For an arbitrary incident angle, main peaks are not observed while side peaks are observed. In order to capture both main and side peaks in one X-ray exposure, the sample was continuously rotated. As a result of this rotation, main peaks become arcs that subtend an angle $2\theta_{h0}$, as shown in Fig. 4.1, with its length equal to $2\theta_{h0}q_{h0}^z$. The detector records the cross sections of these arcs
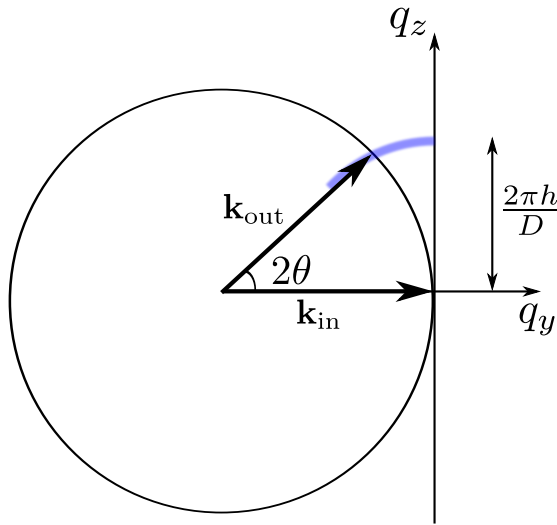

Figure 4.1: caption goes here

36

with the Ewald sphere, so the total scattering power is the product of the observed intensity, I_{hk}^{obs} with the arc length, that is,

$$I = 2\theta_{h0}q_{h0}^z I_{h0}^{\text{obs}}. \tag{4.15}$$

Because the sample has in-plane rotational symmetry, side peaks are represented as rings whose radius is q_{hk}^r. For a fixed incident angle, all the rings are intersected by the Ewald sphere. Because only the domains with the right ripple direction can satisfy the Bragg's condition at a given fixed angle, the scattering power of this small cross section is reduced by a factor of $2\pi q_k^r$ compared to main peaks. During an X-ray exposure, the rings cross the Ewald sphere at all incident angles. Then, the total scattering power is given by

$$I = 2\pi q_k^r I_k^{\text{obs}}. \tag{4.16}$$

Inverting Eq. (4.15) and (4.16) and realizing that the intensity is the form factor squared, we can calculate the observed intensity, I^{obs}, from a model for an electron density in the ripple phase.

Mathematically, the rotation is equivalent to an integration over ω. In low angle X-ray scattering, q_z is constant at a given pixel as ω is changed, which can be seen from Eq. (4.14). ω dependence appears only through q_y, so rotating the sample is realized by integrating over q_y. To derive the integration limits, let us consider two cases: (a) When $\omega \leq 0$, the incoming X-ray beam is blocked by the back of the substrate. This sets the lower limit to 0. (b) When $\omega \geq 2\theta$, the substrate blocks the outgoing X-ray. Within the small angle approximation, then, ω_{max} is $2 \times \lambda q_z/(4\pi)$ for scattering with q_z. Thus, the integration limits for q_y integration are $[-\lambda q_z^2/(4\pi), \lambda q_z^2/(4\pi)]$. We also need to integrate over X and Z to obtain integrated intensity. These lead to the observed intensity written as,

$$I_{hk}^{\text{obs}} \propto \int dX \int dZ \int d\omega |F_{hk}|^2 S_{hk}(\mathbf{q})$$

$$\propto |F_{hk}|^2 \int dq_x \int dq_z \int_{-\frac{\lambda q_z^2}{4\pi}}^{\frac{\lambda q_z^2}{4\pi}} \frac{dq_y}{q_z} S_{hk}(\mathbf{q}), \tag{4.17}$$

where $1/q_z$ factor in q_y integration is the Lorentz polarization factor in the small angle approximation.

For a crystalline sample with the in-plane rotational symmetry, the structure factor is

$$S_{hk}(\mathbf{q}) = S_{hk}(q_r, q_z) = \frac{1}{2\pi q_r}\delta(q_r - q_{r,k})\delta(q_z - q_{z,hk}), \tag{4.18}$$

where $q_{r,k} = 2\pi|k|/\lambda_r$. Thus, the scattering pattern in the ripple phase is a collection of Bragg "rings" centered at the meridian and the Bragg peaks that are called the main peaks.

The observed, integrated intensity of hk peak is proportional to

$$I_{\text{o},hk} \propto \frac{|F_{hk}|^2}{q_{z,hk}} \int dq_x \int_{-q_{y0}}^{q_{y0}} dq_y \frac{\delta(q_r - q_{r,k})}{2\pi q_r}, \qquad (4.19)$$

where $q_{y0} = \lambda q_{z,hk}^2/(4\pi)$. For side peaks ($k \neq 0$), we have

$$\int dq_x \int_{-q_{y0}}^{q_{y0}} dq_y \frac{\delta(q_r - q_{r,k})}{2\pi q_r} \approx \int_{-\frac{q_{y0}}{q_{r,k}}}^{\frac{q_{y0}}{q_{r,k}}} d\phi \int dq_r\, q_r \frac{\delta(q_r - q_{r,k})}{2\pi q_r}$$

$$= \frac{q_{y0}}{\pi q_{r,k}}. \qquad (4.20)$$

For main peaks ($k = 0$), we have

$$\int dq_x \int_{-q_{y0}}^{q_{y0}} dq_y \frac{\delta(q_r - q_{r,k})}{2\pi q_r} = \int_0^{2\pi} d\phi \int dq_r\, q_r \frac{\delta(q_r - q_{r,k})}{2\pi q_r}$$

$$= 1 \qquad (4.21)$$

Using Eq. (4.20) and (4.21), we write the observed integrated intensity as

$$I_{\text{o},h0} \propto \frac{|F_{h0}|^2}{q_{z,h0}} \qquad (4.22)$$

$$I_{\text{o},hk} \propto \frac{|F_{hk}|^2}{q_{z,hk}} \frac{q_{y0}}{\pi q_{r,k}} = |F_{hk}|^2 \frac{\lambda q_{z,hk}}{2\pi} \frac{1}{2\pi q_{r,k}} = |F_{hk}|^2 \frac{2\theta_{hk}}{2\pi q_{r,k}}, \qquad (4.23)$$

where $2\theta_{hk} = \lambda q_{z,hk}/(2\pi)$ is the incident angle at which the outgoing X-ray for the peak (hk) is blocked by the substrate. Eq. (4.22) and (4.23) relate the form factor calculated from a model to the experimentally observed intensity, and are equivalent to Eq. (4.15) and (4.16), which were derived by using the Ewald sphere.

In nonlinear least-squares fitting procedure, we fitted the observed integrated intensity to the calculated intensity from a bilayer model using these geometrical corrections. This is because we can determine experimental uncertainties on observed intensity rather than the geometrically corrected form factors. We avoid propagating the uncertainties by fitting a model to observed intensity.

4.6 Contour Part of the Form Factor

As in ref, we take the ripple profile to have a sawtooth-like profile. Its amplitude is $A/2$ and the projection of the major arm on the ripple direction is x_0 as shown in Fig. X. Then, we write the ripple profile as

$$u(x) = \begin{cases} -\frac{A}{\lambda_r - x_0}\left(x + \frac{\lambda_r}{2}\right) & \text{for} \quad -\frac{\lambda_r}{2} \leq x < -\frac{x_0}{2}, \\ \frac{A}{x_0}x & \text{for} \quad -\frac{x_0}{2} \leq x \leq \frac{x_0}{2}, \\ -\frac{A}{\lambda_r - x_0}\left(x - \frac{\lambda_r}{2}\right) & \text{for} \quad \frac{x_0}{2} < x \leq \frac{\lambda_r}{2}. \end{cases} \qquad (4.24)$$

The ripple profile has the inversion symmetry, so that the resulting form factor is real. A and x_0 are fitting parameters that depend on the integrated intensity of each peak while D and λ_r are determined from measuring the positions of the Bragg peaks.

In order to allow the electron density along the ripple direction to modulate, we include two additional parameters, one to allow for the electron density across the minor side to be different by a ratio f_1 from the electron density across the major side and a second parameter f_2, which is multiplied by δ functions $\delta(x \pm x_0/2)$ to allow for a different electron density near the kink between the major and the minor sides.

4.7 Transbilayer Part of the Form Factor

4.7.1 Delta Function Model

4.7.2 2G Hybrid Model

In the hybrid model, the terminal methyl region of the bilayer is represented as a Gaussian function [9]. The headgroups are represented by one and two Gaussian functions in 1G and 2G hybrid model, respectively. The methylene and water regions are each treated as a constant. The gap between the two constants is represented by a sine function. Then, for half of the bilayer, $0 \leq z \leq D/2$, the electron density has the form,

$$\rho(z) = \rho_{\mathrm{G}}(z) + \rho_{\mathrm{S}}(z) + \rho_{\mathrm{B}}(z), \tag{4.25}$$

where the Gaussian part is given by

$$\rho_{\mathrm{G}}(z) = \sum_{i=1}^{1 \text{ or } 2} \rho_{\mathrm{H}i} e^{-(z - Z_{\mathrm{H}i})^2 / (2\sigma_{\mathrm{H}i}^2)} + \rho_{\mathrm{M}} e^{-z^2 / (2\sigma_{\mathrm{M}}^2)}, \tag{4.26}$$

the strip part is given by

$$\rho_{\mathrm{S}}(z) = \begin{cases} \rho_{\mathrm{CH}_2} & \text{for} \quad 0 \leq z < Z_{\mathrm{CH}_2}, \\ \rho_{\mathrm{W}} & \text{for} \quad Z_{\mathrm{W}} \leq z \leq D/2, \end{cases} \tag{4.27}$$

and the bridging part is given by

$$\rho_{\mathrm{B}}(z) = \frac{\rho_{\mathrm{W}} - \rho_{\mathrm{CH}_2}}{2} \cos\left[\frac{-\pi}{\Delta Z_{\mathrm{H}}} (z - Z_{\mathrm{W}}) \right] + \frac{\rho_{\mathrm{W}} + \rho_{\mathrm{CH}_2}}{2} \quad \text{for} \quad Z_{\mathrm{CH}_2} < z < Z_{\mathrm{W}}. \tag{4.28}$$

with $\Delta Z_{\mathrm{H}} = Z_{\mathrm{W}} - Z_{\mathrm{CH}_2}$. Here, we assume $Z_{\mathrm{H}2} > Z_{\mathrm{H}1}$. Table 4.1 shows some of the definitions. The transbilayer profile along $x = -z \tan \psi$ can be obtained by rotating the coordinates x and z by ψ in the clockwise direction and reexpressing $\rho(z)$ in terms of the rotated coordinates. This leads to replaincg x with $x' = x \cos \psi + z \sin \psi$ and z with $z' = -x \sin \psi + z \cos \psi$. Then, the rotated transbilayer profile is

$$\rho(x, z) = \delta(x + z \tan \psi)[\rho_{\mathrm{G}}(z') + \rho_{\mathrm{S}}(z') + \rho_{\mathrm{B}}(z')]. \tag{4.29}$$

	1G	2G
Z_{CH_2}	$Z_{H1} - \sigma_{H1}$	$Z_{H1} - \sigma_{H1}$
Z_W	$Z_{H1} + \sigma_{H1}$	$Z_{H2} + \sigma_{H2}$

Table 4.1: Definitions of Z_{CH_2} and Z_W

Taking the two dimensional Fourier transform of Eq. (4.29) leads to the transbilayer part of the form factor,

$$F_T = \int_{-\frac{D}{2}}^{\frac{D}{2}} \int_{-\frac{\lambda_r}{2}}^{\frac{\lambda_r}{2}} [\rho(x,z) - \rho_W] e^{i(q_x x + q_z z)} dx dz \qquad (4.30)$$

$$= F_G + F_S + F_B. \qquad (4.31)$$

The form factor is calculated in the minus fluid convention, where the bilayer electron density is measured with respect to the electron density of the surrounding solvent. The expression for F_T is rather messy and not shown. The derivation and full expression can be found in the appendix. Here, we note that the fitting parameters in this model are Z_{Hi}, σ_{Hi}, and R_{HiM} for each of the two headgroup Gaussian functions, σ_M for the terminal methyl Gaussian, ΔR for the methylene region, ψ for the lipid tilt, and an overall scaling factor. The contour part of the form factor has four more parameters (A, x_0, f_1, and f_2). In total, the modified 2G hybrid model implements 14 structural parameters.

4.8 Results

4.9 Data

Table 4.2 summarizes data we analyzed. As shown, we measured scattering in a

	λ_r	D	γ
WW	141.7	57.94	98.4°
S1	145	57.8	98.2°
S2	?	?	?

Table 4.2: Lattice constants

almost identical conditions as the Wack and Webb's. This data allowed us to check our data obtained by using an oriented sample against an unoriented sample. As discussed earlier, these two types of samples give different Lorentz correction. We derived the Lorentz correction for our oriented sample. Applying the derived correction to our data and calculating the form factor, we were able to confirm our correction. This check is shown in Table.

Figure shows a LAXS pattern from DMPC at 18 °C. $D = 57.9$ Å. Low resolution experiment. Up to $h = 9$ orders were observed in this data set. Because of a non-negligible degree of mosaicity in the sample, strong orders cast their arcs over weaker orders. A care must be taken to decompose the intensity at a given pixel to intensity due to a strong order's arc and to that due to a weak peak. This was achieved by taking a q_z swath and fitting the intensity to two Gaussian functions whose widths were determined from the known instrumental resolution. Figure shows an example of this operation. Table and Table show with and without the decomposition operation, respectively. For many of the orders observed, errors one would expect from neglecting the mosaicity effect were small. For higher orders, however, this was crucial to obtain the correct integrated intensity.

In order to test the decomposition effect, fits were also performed for the sum of intensity for orders that overlap.

First, we fitted the data using only up to $h = 3$ orders. What did we get? How did each model do? Any inconsistency witht Sun PNAS?

Next, we fitted every peak we observed. Which model failed?

4.10   Electron Density Profile

Table X shows the best fit for each model. It shows that the delta function model fails. Its failure is obviously due to its lack of fine structural details. In ref. (SUN), the model marginally worked because only up to the third orders were available. With the high flux synchrotron X-ray beam, many more higher orders were observed, whose intensity is dominated by finer details in the bilayer electron density. The table shows that 1G model also fails. 2G model works, but simple 2G model failed. $k = 6$ orders clearly require the modulation in the electron density along the ripple direction. The phase of lower orders tends to be the same throughout the different models while higher orders vary widely. These are just ideas. I need to do actual fitting.

4.11   Discussion

Comparison with previous unoriented/oriented stuff?

Which theories are consistent/inconsistent with the results of this study?

4.12   Conclusion

Well, the ripple phase is the greatest phase in the lipid bilayers. Our detailed work lead to deeper insight into the formation of this phase. Future experiments include the high resolution transmission experiment, where both geometric broadening and

energy dispersion are minimized. The expected resolution is the width of the X-ray beam, which is about 3 pixels. This experiment doubles the best resolution achieved in this work. Another slightly different high resolution experiment is to use silicon crystal analyzer downstread of the sample, which completely remove geoemtric boradening. The downside of this type of high resolution experiment is that only one point in q-space is probed at any given exposure, so to get a full 2D map of wide angle scattering is time consuming.

Appendices

Appendix A

Tat

Appendix B

Ripple Phase

B.1 Rotation of a Two-Dimensional Function

Let us consider rotating a function, $f(x, z)$ in two dimensions by an angle, ψ, in the counterclockwise direction (see Fig. X). This is easily achieved by rotating the coordinate system by ψ in the clockwise direction. Let rotated coordinates be x' and z'. A point in the original coodinates, (x, z), is written as (x', z') in the new coordinates. More specifically, the point P is written as $\mathbf{P} = x\hat{\mathbf{x}} + z\hat{\mathbf{z}} = x'\hat{\mathbf{x}}' + z'\hat{\mathbf{z}}'$. $\hat{\mathbf{x}}$ and $\hat{\mathbf{z}}$ in the $x'z'$ coordinate system are written as

$$\hat{\mathbf{x}} = \cos\psi\hat{\mathbf{x}}' + \sin\psi\hat{\mathbf{z}}' \tag{B.1}$$

$$\hat{\mathbf{z}} = -\sin\psi\hat{\mathbf{x}}' + \cos\psi\hat{\mathbf{z}}'. \tag{B.2}$$

Pluggin these in $\mathbf{P} = x\hat{\mathbf{x}} + z\hat{\mathbf{z}}$ leads to

$$x' = x\cos\psi - z\sin\psi \tag{B.3}$$

$$z' = z\cos\psi + x\sin\psi, \tag{B.4}$$

the inverse of which is

$$x = x'\cos\psi + z'\sin\psi \tag{B.5}$$

$$z = -x'\sin\psi + z'\cos\psi. \tag{B.6}$$

Using the latter equations, $f(x, z)$ can be expressed in terms of x' and z'. The resulting function $f(x', z')$ is the rotated version of $f(x, z)$.

As an example, let us consider a Dirac delta function located at $(x, z) = (0, Z_{H)}$, that is, $f(x, z) = \delta(x)\delta(z - Z_{H)}$. After the rotation by ψ, it becomes

$$f(x, z) \rightarrow \delta(x\cos\psi + z\sin\psi)\delta(-x\sin\psi + z\cos\psi - Z_{H)}$$

$$= \frac{\delta(x + z\tan\psi)}{|\cos\psi|}\frac{\delta(-x\sin\psi\cos\psi + z\cos^2\psi - Z_{H\cos}\psi)}{1/|\cos\psi|}$$

$$= \delta(x + z\tan\psi)\delta(z\tan\psi\sin\psi\cos\psi + z\cos^2\psi - Z_{H\cos}\psi)$$

$$= \delta(x + z\tan\psi)\delta(z - Z_{H\cos}\psi),$$

which is a part of the expression for $T_\psi(x, z)$ in the simple delta function model.

B.2 Derivation of the transbilayer part of the form factor in the 2G hybrid model

In this section, we derive the trasbilayer part of the form factor calculated from the 2G hybrid model discussed in section X. Defining $z' = -x \sin \psi + z \cos \psi$, the Fourier transform of a Gaussian function along the line tilted from z-axis by ψ is

$$
\iint dz\, dx\, \rho_{\mathrm{H}i} \exp\left\{ -\frac{(z' - Z_{\mathrm{H}i})^2}{2\sigma_{\mathrm{H}i}^2} \right\} \delta(x \cos \psi + z \sin \psi) e^{iq_x x} e^{iq_z z}
$$

$$
= \frac{1}{\cos \psi} \int_{-\frac{D}{2}}^{\frac{D}{2}} dz\, \rho_{\mathrm{H}i} \exp\left\{ -\frac{(z - Z_{\mathrm{H}i} \cos \psi)^2}{2\sigma_{\mathrm{H}i}^2 \cos^2 \psi} + i(q_z - q_x \tan \psi) z \right\}
$$

$$
\approx \rho_{\mathrm{H}i} \sqrt{2\pi} \sigma_{\mathrm{H}i} \exp\left\{ i\alpha Z_{\mathrm{H}i} - \frac{1}{2}\alpha^2 \sigma_{\mathrm{H}i}^2 \right\} \tag{B.7}
$$

with $\alpha = q_z \cos \psi - q_x \sin \psi$. Using Eq. (B.7) and adding the other side of the bilayer and the terminal methyl term, we get

$$
F_{\mathrm{G}} = \sqrt{2\pi} \left[-\rho_{\mathrm{M}} \sigma_{\mathrm{M}} \exp\left\{ -\frac{1}{2}\alpha^2 \sigma_{\mathrm{M}}^2 \right\} \right.
$$

$$
\left. + \sum_{i=1}^{1 \text{ or } 2} 2\rho_{\mathrm{H}i} \sigma_{\mathrm{H}i} \cos(\alpha Z_{\mathrm{H}i}) \exp\left\{ -\frac{1}{2}\alpha^2 \sigma_{\mathrm{H}i}^2 \right\} \right]. \tag{B.8}
$$

The strip part of the model in the minus fluid convention is

$$
\rho_{\mathrm{S}}(z) = \begin{cases} -\Delta\rho & \text{for} \quad 0 \le z < Z_{\mathrm{CH}_2} \cos \psi, \\ 0 & \text{for} \quad Z_{\mathrm{W}} \cos \psi \le z \le D/2, \end{cases} \tag{B.9}
$$

where $\Delta\rho = \rho_{\mathrm{W}} - \rho_{\mathrm{CH}_2}$. Then, the corresponding Fourier transform is

$$
F_{\mathrm{S}} = \iint dz\, dx\, e^{iq_x x} e^{iq_z z} \rho_{\mathrm{S}}(z) \delta(x \cos \psi + z \sin \psi)
$$

$$
= \frac{2}{\cos \psi} \int_0^{Z_{\mathrm{CH}_2} \cos \psi} dz \cos\left(\frac{\alpha}{\cos \psi} z \right)(-\Delta\rho)
$$

$$
= -2\Delta\rho \frac{\sin(\alpha Z_{\mathrm{CH}_2})}{\alpha}. \tag{B.10}
$$

The bridging part of the model in the minus fluid convention is

$$
\rho_{\mathrm{B}}(x, z) = \frac{\Delta\rho}{2} \cos\left[\frac{-\pi}{\Delta Z_{\mathrm{H}}}(z' - Z_{\mathrm{W}}) \right] - \frac{\Delta\rho}{2} \tag{B.11}
$$

for $Z_{CH_2} \cos\psi < z < Z_W \cos\psi$, and 0 otherwise. Here, $\Delta Z_H = Z_W - Z_{CH_2}$. Then, for the strip part of the form factor, we have

$$
\begin{aligned}
F_B &= \iint dz\, dx\, e^{iq_x x} e^{iq_z z} \delta(x\cos\psi + z\sin\psi)\rho_B(x,z) \\
&= \frac{\Delta\rho}{\cos\psi} \int_{Z_{CH_2}\cos\psi}^{Z_W\cos\psi} dz \cos\left(\alpha\frac{z}{\cos\psi}\right)\left\{\cos\left[-\frac{\pi}{\Delta Z_H}\left(\frac{z}{\cos\psi} - Z_W\right)\right] - 1\right\} \\
&= \Delta\rho\left\{\frac{\Delta Z_H \sin\left[\frac{\pi(-u+Z_W)}{\Delta Z_H} + \alpha u\right]}{-2\pi + 2\alpha\Delta Z_H} + \frac{\Delta Z_H \sin\left[\frac{\pi(u-Z_W)}{\Delta Z_H} + \alpha u\right]}{2\pi + 2\alpha\Delta Z_H} - \frac{\sin(\alpha u)}{\alpha}\right\}\Bigg|_{Z_{CH_2}}^{Z_W} \\
&= -\frac{\Delta\rho}{\alpha}\left[\sin(\alpha Z_W) - \sin(\alpha Z_{CH_2})\right] \\
&\quad + \frac{\Delta\rho}{2}\left(\frac{1}{\alpha + \frac{\pi}{\Delta Z_H}} + \frac{1}{\alpha - \frac{\pi}{\Delta Z_H}}\right)\left[\sin(\alpha Z_W) + \sin(\alpha Z_{CH_2})\right]. \tag{B.12}
\end{aligned}
$$

Because our X-ray scattering intensity was measured in a relative scale, an overall scaling factor was necessary for a non linear least square fitting procedure. This means that $\Delta\rho$ can be absorbed in the scaling factor. Doing so means that the values of ρ_{Hi} and ρ_M resulting from a fitting procedure are relative to $\Delta\rho$. One way to have these parameters in the absolute scale is to integrate the bilayer electron density over the lipid volume and equate the result to the total number of electrons in the lipid, which can easily be calculated from the chemical formula. For the ripple phase study in this thesis, the absolute values of the electron density were not of importance, so the discussion was omitted in the main text.

B.3 Derivation of the contour part of the form factor

In this section, we derive F_C. The ripple profile, $u(x)$ is given by

$$
u(x) = \begin{cases}
-\frac{A}{\lambda_r - x_0}\left(x + \frac{\lambda_r}{2}\right) & \text{for} \quad -\frac{\lambda_r}{2} \le x < -\frac{x_0}{2} \\
\frac{A}{x_0}x & \text{for} \quad -\frac{x_0}{2} \le x \le \frac{x_0}{2} \\
-\frac{A}{\lambda_r - x_0}\left(x - \frac{\lambda_r}{2}\right) & \text{for} \quad \frac{x_0}{2} < x \le \frac{\lambda_r}{2}
\end{cases} \tag{B.13}
$$

The contour part of the form factor is the Fourier transform of the contour function, $C(x,z)$,

$$
F_C(\mathbf{q}) = \frac{1}{\lambda_r} \int_{-\frac{\lambda_r}{2}}^{\frac{\lambda_r}{2}} dx \int_{-\frac{D}{2}}^{\frac{D}{2}} dz\, C(x,z) e^{iq_z z} e^{iq_x x}
$$

As discussed in section X, the modulated models allow the electron density to modulate along the ripple direction, x. This means

$$C(x, z) = \begin{cases} f_1 \delta[z - u(x)] & \text{for} \quad -\frac{\lambda_r}{2} \leq x < -\frac{x_0}{2} \\ \delta[z - u(x)] & \text{for} \quad -\frac{x_0}{2} < x < \frac{x_0}{2} \\ f_1 \delta[z - u(x)] & \text{for} \quad \frac{x_0}{2} \leq x < \frac{\lambda_r}{2} \end{cases}$$

$$+ f_2 \, \delta\left(x + \frac{x_0}{2}\right) \delta\left(z + \frac{A}{2}\right) + f_2 \, \delta\left(x - \frac{x_0}{2}\right) \delta\left(z - \frac{A}{2}\right). \tag{B.14}$$

The contribution from the minor arm is

$$\frac{1}{\lambda_r} \int_{-\frac{\lambda_r}{2}}^{-\frac{x_0}{2}} dx \, e^{iq_x x} e^{iq_z u(x)} + \int_{\frac{x_0}{2}}^{\frac{\lambda_r}{2}} dx \, e^{iq_x x} e^{iq_z u(x)}$$

$$= \frac{1}{\lambda_r} \int_{\frac{x_0}{2}}^{\frac{\lambda_r}{2}} dx \, e^{-i\left[q_x x - q_z \frac{A}{\lambda_r - x_0}\left(x - \frac{\lambda_r}{2}\right)\right]} + \int_{\frac{x_0}{2}}^{\frac{\lambda_r}{2}} dx \, e^{i\left[q_x x - q_z \frac{A}{\lambda_r - x_0}\left(x - \frac{\lambda_r}{2}\right)\right]}$$

$$= \frac{2}{\lambda_r} \int_{\frac{x_0}{2}}^{\frac{\lambda_r}{2}} \cos\left[\left(q_x - q_z \frac{A}{\lambda_r - x_0}\right)x + q_z \frac{A}{\lambda_r - x_0} \frac{\lambda_r}{2}\right] \tag{B.15}$$

Using a trigonometric identity,

$$\sin u - \sin v = 2 \cos[(u + v)/2] \sin[(u - v)/2],$$

and defining

$$\omega(\mathbf{q}) = \frac{1}{2} \left(q_x x_0 + q_z A\right), \tag{B.16}$$

we further simplify Eq. (B.15),

$$= \frac{2}{\lambda_r} \frac{\lambda_r - x_0}{\frac{1}{2} q_x \lambda_r - \omega} \cos\left[\frac{1}{2}\left(\frac{1}{2} q_x \lambda_r + \omega\right)\right] \sin\left[\frac{1}{2}\left(\frac{1}{2} q_x \lambda_r - \omega\right)\right]$$

$$= \frac{1}{\lambda_r} \frac{\lambda_r - x_0}{\frac{1}{2} q_x \lambda_r - \omega} \cos\left[\frac{1}{2}\left(\frac{1}{2} q_x \lambda_r + \omega\right)\right] \frac{\sin\left(\frac{1}{2} q_x \lambda_r - \omega\right)}{\cos\left[\frac{1}{2}\left(\frac{1}{2} q_x \lambda_r - \omega\right)\right]}$$

$$= \frac{\lambda_r - x_0}{\lambda_r} \frac{\cos\left[\frac{1}{2}\left(\frac{1}{2} q_x \lambda_r + \omega\right)\right]}{\cos\left[\frac{1}{2}\left(\frac{1}{2} q_x \lambda_r - \omega\right)\right]} \frac{\sin\left(\frac{1}{2} q_x \lambda_r - \omega\right)}{\frac{1}{2} q_x \lambda_r - \omega}. \tag{B.17}$$

Similarly, we calculate the contribution from the major arm,

$$\frac{1}{\lambda_r} \int_{-\frac{x_0}{2}}^{\frac{x_0}{2}} dx \, e^{i\left(\frac{q_z A}{x_0} + q_x\right)x} = \frac{2}{\lambda_r} \int_0^{\frac{x_0}{2}} dx \cos\left(\frac{q_z A}{x_0} + q_x\right)x$$

$$= \frac{x_0}{\lambda_r} \frac{\sin \omega}{\omega} \tag{B.18}$$

The contribution from the kink region is

$$\frac{1}{\lambda_r} \iint dx \, dz \left[\delta\left(x + \frac{x_0}{2}\right)\delta\left(z + \frac{A}{2}\right) + \delta\left(x - \frac{x_0}{2}\right)\delta\left(z - \frac{A}{2}\right) \right] e^{iq_x x} e^{iq_z z}$$

$$= \frac{2}{\lambda_r} \cos \omega. \tag{B.19}$$

Therefore,

$$F_C(\mathbf{q}) = \frac{x_0}{\lambda_r}\frac{\sin \omega}{\omega} + f_1 \frac{\lambda_r - x_0}{\lambda_r}\frac{\cos\left[\frac{1}{2}\left(\frac{1}{2}q_x\lambda_r + \omega\right)\right]}{\cos\left[\frac{1}{2}\left(\frac{1}{2}q_x\lambda_r - \omega\right)\right]}\frac{\sin\left(\frac{1}{2}q_x\lambda_r - \omega\right)}{\frac{1}{2}q_x\lambda_r - \omega}$$

$$+ \frac{2f_2}{\lambda_r}\cos \omega \tag{B.20}$$

B.4 Correction due to refractive index

q_z needs be corrected for index of refraction. Let θ' and λ' be the true scattering angle and wavelength within the sample. The wavelength by an energy analyzer, λ, and the scattering angle calculated from a position on a CCD detector, θ are apparent. The correction is not necessary in the horizontal direction. The Snell's law in Fig. X gives

$$n \cos \theta = n' \cos \theta' \tag{B.21}$$

$$n\lambda = n'\lambda'. \tag{B.22}$$

For low angle X-ray scattering, the momentum transfer along z direction is

$$q_z = \frac{4\pi \sin \theta'}{\lambda'} \tag{B.23}$$

$$= \frac{4\pi n'}{n\lambda}\sin \theta' \tag{B.24}$$

$$= \frac{4\pi n'}{n\lambda}\sqrt{1 - \cos^2 \theta'} \tag{B.25}$$

$$= \frac{4\pi n'}{n\lambda}\sqrt{1 - \left(\frac{n}{n'}\cos \theta\right)^2}. \tag{B.26}$$

The apparent scattering angle, θ, is directly related to the vertical pixel position, p_z, by

$$\theta = \frac{1}{2}\tan^{-1}\left(\frac{p_z}{S}\right), \tag{B.27}$$

where S is the sample-to-detector distance. The typical units of S and p_z are in mm. In our experimental setup, $n = 1$ and $n' = 0.9999978$ for lipids at $\lambda = 1.18$ Å.

Bibliography

[1] Norbert Kuerka, John F. Nagle, Jonathan N. Sachs, Scott E. Feller, Jeremy Pencer, Andrew Jackson, and John Katsaras. Lipid bilayer structure determined by the simultaneous analysis of neutron and x-ray scattering data. *Biophysical Journal*, 95(5):2356 – 2367, 2008.

[2] Stephanie Tristram-Nagle, Yufeng Liu, Justin Legleiter, and John F. Nagle. Structure of gel phase DMPC determined by x-ray diffraction. *Biophysical Journal*, 83(6):3324 – 3335, 2002.

[3] Anthony R. Braun, Jonathan N. Sachs, and John F. Nagle. Comparing simulations of lipid bilayers to scattering data: The gromos 43a1-s3 force field. *The Journal of Physical Chemistry B*, 117(17):5065–5072, 2013.

[4] Berk Hess, Carsten Kutzner, David van der Spoel, and Erik Lindahl. Gromacs 4: Algorithms for highly efficient, load-balanced, and scalable molecular simulation. *Journal of Chemical Theory and Computation*, 4(3):435–447, 2008.

[5] Joakim P. M. Jmbeck and Alexander P. Lyubartsev. Derivation and systematic validation of a refined all-atom force field for phosphatidylcholine lipids. *The Journal of Physical Chemistry B*, 116(10):3164–3179, 2012.

[6] Joakim P. M. Jmbeck and Alexander P. Lyubartsev. An extension and further validation of an all-atomistic force field for biological membranes. *Journal of Chemical Theory and Computation*, 8(8):2938–2948, 2012.

[7] Viktor Hornak, Robert Abel, Asim Okur, Bentley Strockbine, Adrian Roitberg, and Carlos Simmerling. Comparison of multiple amber force fields and development of improved protein backbone parameters. *Proteins: Structure, Function, and Bioinformatics*, 65(3):712–725, 2006.

[8] `http://henke.lbl.gov/optical_constants`.

[9] M.C. Wiener, R.M. Suter, and J.F. Nagle. Structure of the fully hydrated gel phase of dipalmitoylphosphatidylcholine. *Biophysical Journal*, 55(2):315 – 325, 1989.